Mon. Not. R. Astron. Soc. **284,** 576–598 (1997)

Stellar proper motions in the central 0.1 pc of the Galaxy

A. Eckart and R. Genzel

Max-Planck-Institut für Extraterrestrische Physik, Giessenbachstraße, D-8046, Garching bei München, Germany

Accepted 1996 September 9. Received 1996 September 6; in original form 1996 August 6

ABSTRACT

We report the first results of a programme to measure proper motions of stars in the innermost core of the Galaxy. From high-resolution near-infrared imaging over the last four years we have determined proper motions for 39 stars between 0.03 and 0.3 pc from the compact radio source Sgr A*. For 19 of these the derived motions are more significant than 4σ in at least one coordinate. Proper motion and radial velocity dispersions are in very good agreement, indicating that the stellar velocity field on average is close to isotropic. Taking radial and proper motion data together the dynamic evidence is now strong that there is a $2.45(\pm 0.4) \times 10^6$-$M_\odot$ central dark mass located within ≤ 0.015 pc of Sgr A*. Its mass density is at least $6.5 \times 10^9\ M_\odot\ pc^{-3}$, excluding the fact that the central mass concentration is in form of a compact white dwarf or neutron star cluster. In addition, we have detected significant changes in the structure of the innermost complex of stars in the immediate vicinity of Sgr A*, implying in at least one case stellar motions of ≥ 1500 km s^{-1} within ~ 0.01 pc of the compact radio source. Including this preliminary evidence, the inferred density of the central dark mass would then have to be in excess of $10^{12}\ M_\odot\ pc^{-3}$, implying that the central mass concentration is probably a single massive black hole.

Key words: astrometry – stars: fundamental parameters – stars: imaging – Galaxy: centre – infrared: general.

1 INTRODUCTION

The question of whether or not galactic nuclei contain central massive black holes is of considerable importance for the understanding of active galactic nuclei and the evolution of galaxies. Probably the most unambiguous way to answer this question is from dynamical measurements (see Kormendy & Richstone 1995 for a review). The Galactic centre is a unique target for searching for a central massive black hole as it is so close (~ 8 kpc, 1 arcsec $\equiv 0.039$ pc, used throughout this paper, Reid 1993) and detailed measurements of gas and stellar dynamics are now possible down to a scale of about 0.01 pc. Evidence for a dark central mass concentration at the core of the Milky Way from observations of radial velocities of gas and stars has been steadily growing over the past two decades (Wollman 1976; Lacy et al. 1980; Lacy, Achterman & Serabyn 1991; Serabyn & Lacy 1985; Genzel et al. 1985, 1996; McGinn et al. 1989; Sellgren et al. 1990; Lindqvist, Habing & Winnberg 1992; Krabbe et al. 1995; Haller et al. 1996). In a recent study of the radial velocities of 222 stars within 1 pc of the dynamic centre, Genzel et al. (1996) found that a central compact (core radius ≤ 0.06 pc) dark mass of 2.2 to $3.2 \times 10^6\ M_\odot$ (for a distance of 8.0 kpc) is required with fairly high significance if the stellar motions are isotropic.

For determining the mass distribution from stellar dynamics without the a priori assumption of isotropic motions, it is necessary to determine both radial and proper motions of the stars. In contrast to external galaxies stellar proper motions in the Galactic centre can realistically be measured in a few years time if relative stellar positions can be determined to about 10 mas. To achieve this goal we have, since 1991, been carrying out a programme of high-resolution 2.2-μm (K band) imaging at the 3.5-m New Technology Telescope (NTT) of the European Southern Observatory (ESO) in La Silla, Chile. Preliminary results on the proper motions in the outer cluster (distances larger than 0.03 pc from Sgr A*) are summarized in Eckart & Genzel (1996). Here we discuss and analyse these outer proper motions in more detail and give the first results for the innermost cluster (with radii less than 1 arcsec) based on seven epochs of images spanning four years.

2 OBSERVATIONS AND ANALYSIS

2.1 Shift-and-add imaging

Using a high-resolution camera developed specifically for this purpose (SHARP: Hofmann et al. 1993), we have applied speckle imaging techniques to obtain diffraction-limited resolution. Techniques and results from the near-infrared imaging have been discussed in several earlier papers (Eckart et al. 1992, 1993, 1994, 1995). Briefly, for each epoch several thousand short-exposure (integration time 0.3 to 0.5 s) frames $I(x,y)$ of the object $O(x,y)$ were taken in very good seeing conditions with a short-exposure seeing of typically 0.3 to 0.8 arcsec. Each short exposure can be written as

$$I(x,y) = O(x,y) * P(x,y) + N(x,y), \quad (1)$$

with $P(x,y)$ being the combined telescope and atmospheric point spread function (PSF) and $N(x,y)$ an additive noise component. These images are then coadded with the simple shift-and-add (SSA) algorithm (Christou 1991). The basic assumption of the SSA algorithm is that individual speckles can be regarded as distorted, diffraction-limited images of the object. For the SSA procedure we use the pixel position x_m, y_m of the brightest speckle with respect to the seeing disc centroid of either IRS7 or IRS16NE, the two brightest stars in the 12.8×12.8 arcsec^2 field of our camera. One pixel is 50 mas in SHARP resulting in three samples per diffraction beam. The resulting SSA image $S(x,y)$ can then be written as

$$S(x,y) = 1/M \sum_{m=1}^{M} I_m(x - x_m, y - y_m). \quad (2)$$

The resulting SSA PSF is a diffraction-limited spike (0.15-arcsec FWHM at 2.2 μm) sitting on top of a smooth seeing background (typical Strehl ratio 0.2). Next we CLEANed the resulting SSA image of typically a few thousand coadded short exposure frames using the Lucy–Richardson (Lucy 1974) algorithm. As a representation of the 'dirty' PSF we used the data of the brightest source in the image (IRS7). After a few thousand iterations of the algorithm the resulting maps consisted of well-separated sources (stars) concentrated in 1 to 4 pixels, depending on their positions. In analogy to the CLEAN algorithm used in radio astronomy we will refer to this image as the 'δ-function map'. This δ-function map is then reconvolved with a Gaussian of FWHM 0.15 arcsec. The final reconvolved images reach K magnitudes of 15 to 16.5, and show $\sim$600 stars in the central 25-arcsec ($\sim$1 pc) diameter field centred on or near Sgr A* (e.g. Eckart et al. 1993, 1995). We have also analysed several of our data sets with other speckle data reduction techniques (recovering phase in Fourier space), such as the Knox–Thompson method (Knox 1976) or the triple correlation algorithm (Lohmann, Weigelt & Wirnitzer 1983). As shown in Eckart et al. (1992, 1994), the final images obtained with the different techniques compare very well, but the combination of the SSA and the Lucy–Richardson algorithm is by far the best in obtaining a high dynamic range ($\geq$8 mag) map of a crowded set of point sources. A key element is that for very good seeing the 3.5-m NTT at 2.2 μm produces short-exposure images with a fairly small number (3 to 5) of bright, long-lived speckles. For the present study we analysed $\sim$65 independent images (henceforth called 'data sets') from seven observing runs in 1992.25, 1992.65, 1993.65, 1994.27, 1995.6, 1996.25 and 1996.43.

2.2 Determination of accurate relative positions

To determine accurate relative stellar positions with our imaging system (1/20 to 1/10 of the diffraction-limited beam) we proceeded as follows. First, for each data set a final PSF was constructed by averaging the five brightest stellar images. Then relative pixel offsets from IRS16NE were determined for each data set by cross-correlating this PSF and the data in the central 5×5 pixel around the peak of each star. While we finally found that the best method was to use the δ-function maps, different data analysis methods starting directly from the raw SSA maps, or various forms of CLEANed images, gave basically identical results for isolated stars or clearly separable doubles. This is shown in Table 1 which lists the dispersions of differences in extracted x- and y-positions between the cross-correlation method on the δ-map and a Gaussian fitting routine operating (a) on the raw SSA, (b) on the Lucy-deconvolved and (c) on the reconvolved Lucy-CLEANed images. For single stars the dispersions between different data reduction methods range between 3 and 20 mas. The worst results are naturally for the raw SSA maps, where distant but strong sources can affect the results through the wings of the PSF. For double stars the dispersions between the different fitting techniques are $\geq$8 mas (excluding SSA). These uncertainties are smaller than or at most comparable to the final astrometric uncertainties (see below).

In the second step all instrumental imaging parameters up to second order are extracted for each individual data set. Here we assumed that the pixel coordinates (x_i, y_i) of the ith star can be written in terms of the corrected offset coordinates $(\Delta x_i, \Delta y_i)$ from the base position as

$$x_i = a_0 + a_1\Delta x_i + a_2\Delta y_i + a_3\Delta x_i^2 + a_4\Delta x_i\Delta y_i + a_5\Delta y_i^2$$

and

$$y_i = b_0 + b_1\Delta x_i + b_2\Delta y_i + b_3\Delta x_i^2 + b_4\Delta x_i\Delta y_i + b_5\Delta y_i^2. \quad (3)$$

The zeroth order is the base position (a_0, b_0), the first order (proportional to Δx and Δy in each coordinate) relates to the camera rotation angle α_r and the pixel scales ρ_x, ρ_y (arcsec pixel^{-1}) and the second-order parameters give the image distortions (proportional to Δx^2, Δy^2 and $\Delta x\,\Delta y$ for each coordinate). The 2×6 instrumental parameters (a_0, $b_0 \ldots a_5$, b_5) were determined for each data set by comparison to a 'reference frame' constructed from the 1994.27 epoch data. The parameters were computed by solving an overdetermined non-linear equation for N reference stars via orthonormalization of the $12 \times N$ matrix. From this analysis we found that the fitted pixel scales and the very

Table 1. Comparison of stellar positions determined with different data reduction methods.

Data reduction technique	σ (10^{-3}") singles	σ (10^{-3}") doubles
Gauss fit-Lucy reconvolved vs. cross-corr.-Lucy-δ	3	8
Gauss fit-Lucy-δ vs. cross-corr.-Lucy-δ	4	9
Gauss fit-raw SSA vs. cross-corr.-Lucy-δ	19	-

small second-order distortion parameters (approximately 10^{-3} of the first-order parameters) differed by less than 0.5 per cent between different data sets so that the main fit parameters were the base position of the N stars and the camera rotation angle. After correction for the instrumental parameters the final position fit errors ranged from 8 to 20 mas per data set for the brighter, isolated stars. These formal fit errors are in fact a good representation of the experimental (non-systematic) errors. This can be seen from Fig. 1, which shows the final derived relative x- and y-positions of 27 stars as a function of time: these coordinates correspond approximately to RA and Dec., respectively. Each black dot in these figure panels represents an individual independent data set. The scatter in the dots for a given epoch is an empirical measure of the experimental position uncertainties. They agree quite well with the fit errors giving confidence in our data reduction method.

2.3 Systematic errors

Our method has in principal the disadvantage that it determines the imaging parameters from the same stellar positions whose changes we are trying to measure. This leads to systematic errors with proper motions depending on which reference star list was chosen. In practice, however, the solutions turned out to be very stable in terms of selection of the N reference stars, as long as $N \approx 20$ to $30 > N_{\rm min} = 6$. The method tends to slightly underestimate the true proper motions, although we found that this effect is no larger than the typical error bars of the proper motions we encountered. The impact of the effect of this reference star list on the derived proper motions is shown in Fig. 2. It shows the derived x- and y-proper motion of a randomly selected star (IRS21) as a function of the composition of the reference star list. Here we allowed our largest and best reference star list (which we used for the results shown below) to randomly vary in length and composition by up to 50 per cent. The parameter solution was then calculated for 100 such lists. The overwhelming majority of the proper motion solutions lies around the value we find on the basis of the best reference stars list (arrows). Note that a quantitative estimate of the systematic errors of the motions cannot be directly determined from the widths of the histograms in Fig. 1, as many of the lists leading to these histograms are clearly non-optimal. The use of a selection of 'sensible' reference lists indicates that the systematic errors in our velocity estimates are typically ± 50 km s^{-1}.

Note that with the exception of the foreground stars IRR1 and IRR2 (e.g. Rosa et al. 1992), colour terms do not enter significantly into our astrometry. The stellar colours are dominated by reddening which is very similar to that for the stars in the central 1 pc. We estimate that differential refraction leads to less than a few mas distortion of the derived positions.

3 RESULTS

3.1 Detection of stellar proper motions in the central ~0.1 pc

In the present analysis we have determined positional changes as a function of time for 39 stars between 0.9 and 8.8 arcsec from Sgr A*. Table 2 lists their properties: K magnitudes, x- (~RA), y- (~Dec.) offsets from Sgr A* (epoch 1994.27), x- (~RA), y- (~Dec.) proper motions (along with their 1σ uncertainties including the systematic errors discussed in the last section), and (wherever available, Genzel et al. 1996) their radial velocities and their identifications. The quality of the data we have obtained can be seen from Figs 1 and 3. Fig. 1 shows position–time diagrams of the derived x- and y-offsets of 27 selected bright and isolated stars as a function of time. Fig. 3 shows the proper motion vectors of stars in the central few arcseconds, superposed on a 2-μm image.

The data in Figs 1 and 3 and Table 2 show that the relative positions of many of the stars in the central ~0.1 pc appear to change monotonically with time. Of the 39 stars listed in Table 2 motions at the $\geq 5\sigma$ level are detected in at least one coordinate for 10 cases and at the $\geq 4\sigma$ level for 19 cases. The 39 stars in Table 2 were drawn from an original list of about 50 stars with K-band magnitudes brighter than about 13.5. This magnitude limit ensured that we were able to get high signal-to-noise ratio detections for each data set. About 12 stars were eliminated from the list because they were either located in a confused region (in particular the IRS13 region, see Eckart et al. 1993, 1995), or because we had coverage of fewer than seven epochs (affecting about six fairly bright stars in the outer parts of the field), or because they did not produce repeatable positions in all seven epochs with proper motion velocity errors ≤ 100 km s^{-1}.

The motions we have detected cannot be due to orbital motion in multiple star systems that are not resolved at 0.15 arcsec resolution. If one takes the average space velocity of the He I stars (~400 km s^{-1}) in Table 2 as an orbital velocity and assumes further that a typical star has a mass of 60 $M_\odot$ (Krabbe et al. 1995) the orbital period of a binary would be about one week, with an orbital radius ~50 $R_\odot$, comparable to the actual photospheric diameters of the He I stars (Krabbe et al. 1995). If this were truly the case there should be large variations of the relative positions within the typically 10 d of a given epoch but no positional changes on a scale of several years. Turning the argument around orbital periods of three or more years at the observed velocities would require unrealistic stellar masses approaching 10^4 $M_\odot$. Variability in two or more stars that are very close in projection may also lead to apparent proper motion. A number of stars indeed appear to show flux variations in our data sets and we thus cannot exclude with absolute certainty that variability may not corrupt the derived motions of a few of the stars in the sample. However, as we have considered only relatively bright isolated stars with seven-epoch coverage and have discarded stars with ≥ 100 km s^{-1} errors (sometimes showing suspicious jumps in their position–time data), we are confident that variability or other 'Christmas tree effects' cannot cause the motions we see. In addition, lunar occultation measurements (Simon et al. 1990; Simons, Hodapp & Becklin 1990) have proven that the brightest members of the IRS16 complex (with the best proper motion data) are very likely single stars.

We thus conclude *that we have detected orbital proper motions of the stars in the central gravitational field.* An immediate important result is that the velocity dispersion is very similar in all three coordinates and hence that *global anisotropy of the stellar motions must be small.* This can be

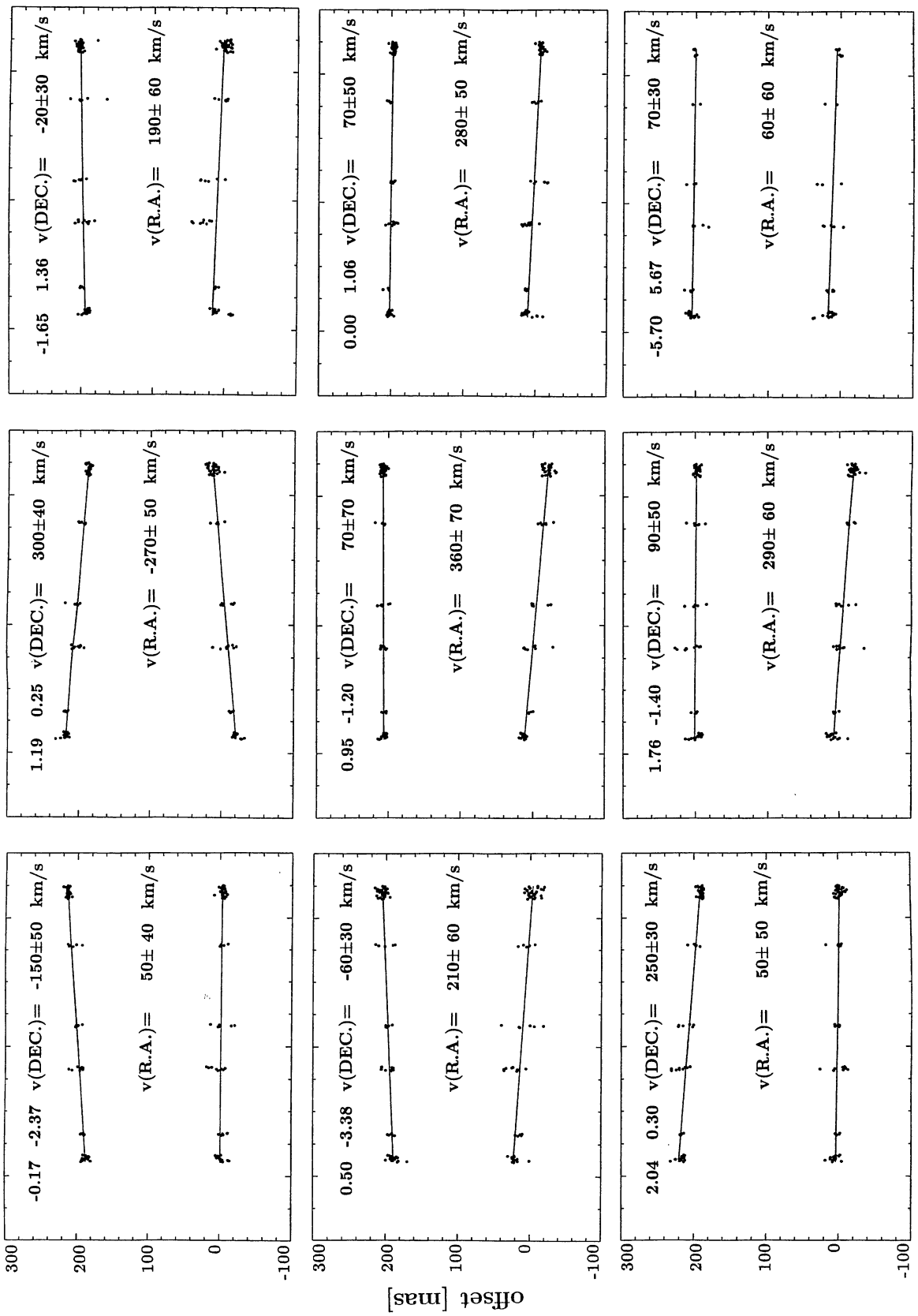

Figure 1. Derived positions as a function of time for 27 of the 39 stars of Table 2. The panels show the x-(~RA) and y-(~Dec.) positions as a function of time, along with the best-fitting proper motions (straight lines). Stars are labelled with their offset coordinates from Sgr A* and the fitted velocities are given. Offsets are relative to the positions determined at the base epoch (1994.27). Positions of the different data sets in each epoch are shown as black dots. For display purposes the graph showing the Dec.-motion has been offset by +200 mas. Fit errors for positions in each data set and the dispersion of fitted positions in an epoch are very similar, indicating largely statistical errors.

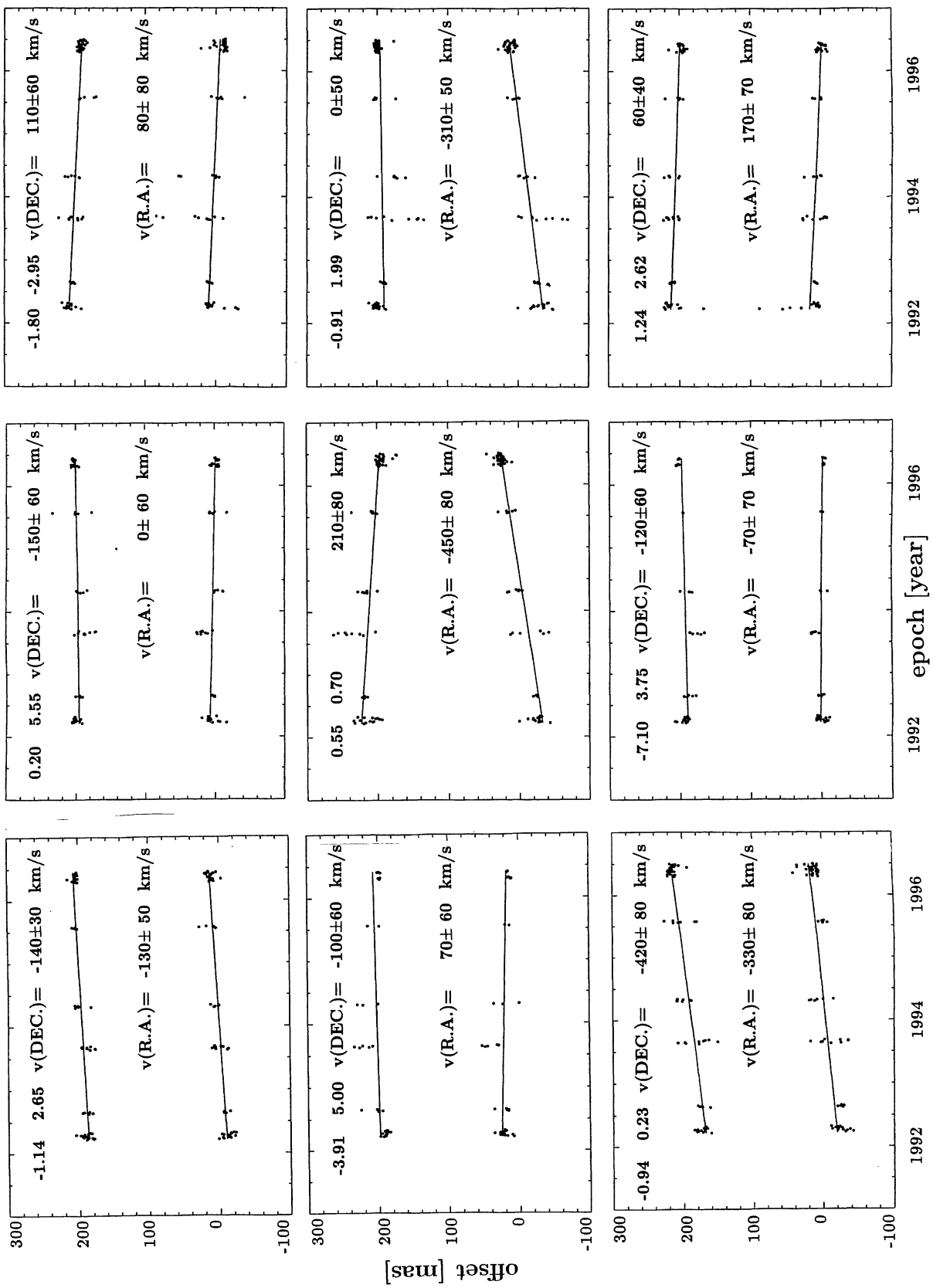

Figure 1 – *continued*

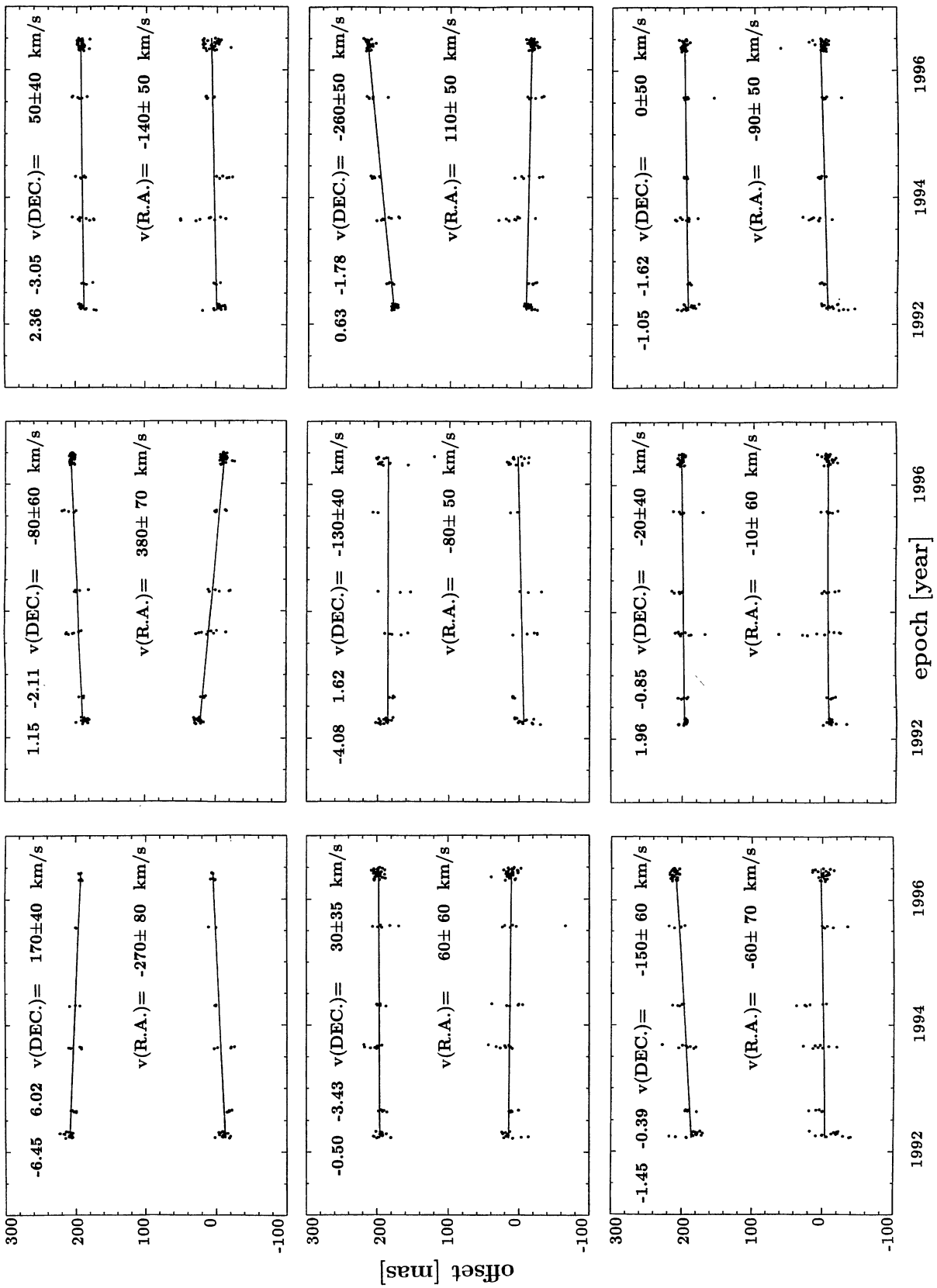

Figure 1 – *continued*

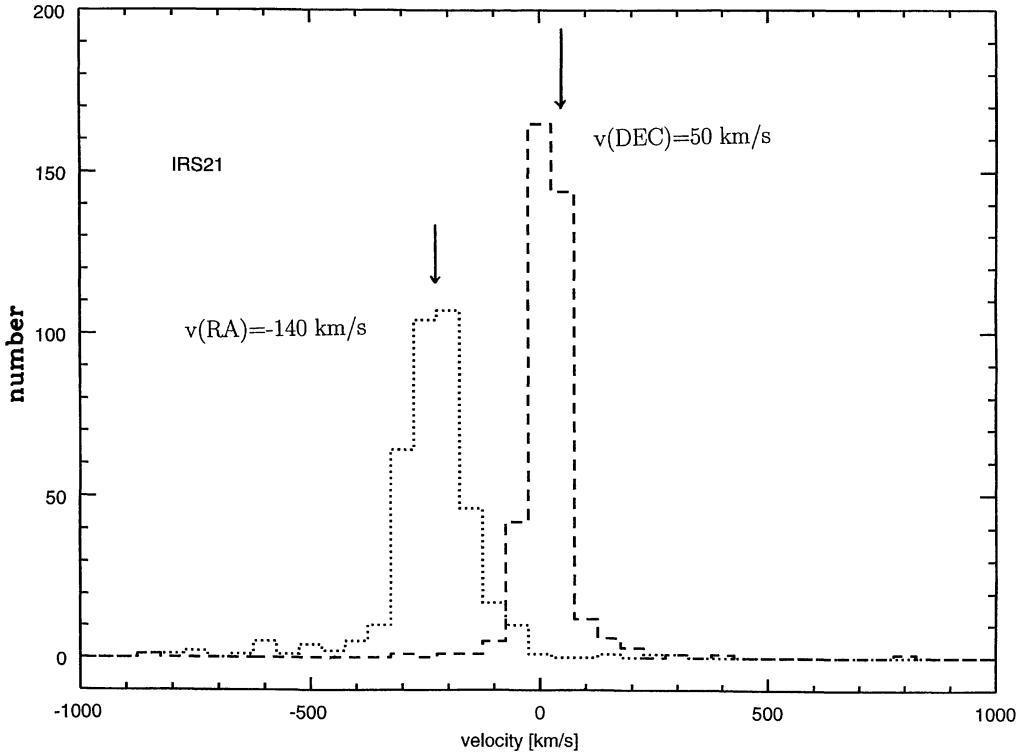

Figure 2. Histogram of the derived x-(~RA) (dotted) and y-(~Dec.) motion (dashed) for IRS21. For each solution the length and composition of the reference star list has been changed. The base reference stars list used for the final solutions (Table 2) was allowed to randomly vary by up to 50 per cent in composition and length. Proper motions were then computed for 100 such lists for the four settings used to map the centre, and the results compared to those of the base list (arrows).

best seen from Fig. 4, where we have plotted proper motion and radial velocity dispersions (from Rieke & Rieke 1988, McGinn et al. 1989, Sellgren et al. 1990, Lindqvist et al. 1992, Genzel et al. 1996, Haller et al. 1996) as a function of projected radius p from Sgr A*. For estimation of the proper motion dispersions (combining x- and y-motions for better statistics), we have divided our sample in Table 2 into three groups. 12 stars (24 motions) between $p=0.8$ and 2.1 arcsec result in a projected velocity dispersion of 214 ± 32 km s^{-1} at $\langle p\rangle=0.057$ pc. 18 stars (36 motions) between 2.1 and 4.1 arcsec give a dispersion of 152 ± 18 km s^{-1} at $\langle p\rangle=0.11$ pc. Nine stars (18 motions) between 4.1 and 8.8 arcsec result in a dispersion of 93 ± 16 km s^{-1} at $\langle p\rangle=0.24$ pc. For the radial velocity dispersion of the early-type stars, a 120 km s^{-1} counter-rotation (which is a very significant global effect for the sample) was first subtracted from the velocities and then statistically re-introduced as an effective radial velocity dispersion ($\sigma^2_{\rm eff}=\sigma^2_{\rm r}+v^2_{\rm rot}/3$, see Genzel et al. 1996). The fact that the innermost radial velocity dispersion of the late-type stars at 0.11 pc ($\sigma_{\rm r}=126\pm23$ km s^{-1}) is lower than either the radial velocity dispersion of the early-type stars or the proper motion dispersion at that radius is very likely due to the central 'hole' in the distribution of late-type stars (Sellgren et al. 1990; Haller et al. 1996; Genzel et al. 1996). Most of the late-type stars seen projected towards the central few arcseconds are actually at much larger radius so that the projected velocity dispersion appears low; after correction for this effect the dispersion would be about 150 km s^{-1}, in agreement with the other two data points. Table 2 shows that the three space velocities are also comparable if we consider only those stars for which all three velocities are available. While these conclusions were obtained by adopting an 8.0-kpc distance to the Galactic Centre, they are unchanged if the range of possible Galactic Centre distances (7.5 to 8.5 kpc: Reid 1993) is used. Taken together the measurements for $p\geq0.057$ pc now show a *very significant Keplerian [$\sigma(p)\sim p^{-0.5}$] fall-off of the stellar velocities with distance from the dynamic centre (assumed to be at Sgr A*), demonstrating fairly convincingly that there must be a central, compact and dark (cf. Genzel et al. 1996) mass concentration.* It is interesting to note that the late-type stars in Table 2 projected within a few arcseconds of Sgr A* have consistently smaller proper motions (and raial velocities, see above) than the early-type stars ('He I') in the same area. This is consistent with the above-mentioned fact (Sellgren et al. 1990; Haller et al. 1996; Genzel et al. 1996) than the distribution of brighter late-type stars has a central hole (equivalent to a large effective core radius). Hence for a given projected radius from the dynamic centre a late-type star will on average be at larger true radius than an early-type star. The smaller proper motions of the late-type stars just discussed thus are an independent confirmation of the drop of stellar velocities with radius.

3.2 Constraints on the mass, location and size of the central dark mass

We now discuss the quantitative constraints that the new data on the mass distribution provide. Fitting to the projected velocity dispersion data in Fig. 4 a model with a

Table 2. Derived stellar velocities.

Source	K-mag	ΔRA (")	ΔDec (")	p_{SgrA^*} (")	v_{RA} (km/s)	v_{Dec} (km/s)	v_{rad} (km/s)	$\|v_{tot}\|$ (km/s)	Stellar type
	12.5	0.55	0.7	0.89	-450±80	210±80		≥500	
	13.5	-0.94	0.23	0.97	-330±80	-420±80		≥530	
16 NW	10	0.00	1.06	1.06	280±50	70±50	-35±70	290	HeI
IRS 16 C	9.5	1.19	0.25	1.22	-270±50	300±40	150±70	430	HeI
	13	-1.45	-0.39	1.50	-60±70	-150±60		≥160	
	13	0.40	1.47	1.52	380±80	40±70		≥380	
16 SW	9.5	0.95	-1.20	1.53	360±70	70±70	400±70	540	HeI
	13	-1.75	-0.6	1.85	0±80	-20±50		≥20	
	11	0.63	-1.78	1.89	110±50	-260±50	-209±30	350	late type
	13	-1.05	-1.62	1.93	-90±50	0±50	100±25	130	late type
16 CC	10.5	2.04	0.30	2.06	50±50	250±30		≥250	HeI?
29 S	11.5	-1.88	0.85	2.06	15±50	210±50	-93±20	230	late type
	11.5	1.96	-0.85	2.14	-10±60	-20±40	-140±30	140	late type
29 N	10	-1.65	1.36	2.14	190±60	-20±30	-110±150	220	HeI
	12	-0.91	1.99	2.19	-310±50	0±50	-20±100	310	HeI
16 SE(1)	11	1.76	-1.40	2.25	290±60	90±50	450±150	540	HeI
	10.5	-0.17	-2.37	2.38	50±40	-150±50		≥160	
	13.5	2.34	-0.54	2.40	-40±70	240±60		≥240	
	10.5	1.15	-2.11	2.40	380±70	-80±60		≥390	
	13	-1.05	-2.30	2.53	-230±50	-70±70		240	
	13	-1.85	-1.78	2.57	120±90	-70±50		≥140	
	12	-1.14	2.65	2.88	-130±50	-140±30	20±30	190	late type
	12.5	1.24	2.62	2.90	170±70	60±40	-100±30	210	late type
	13	-1.86	-2.37	3.01	-90±60	70±40		≥110	
16 NE	9	2.90	0.90	3.04	250±90	-500±90	10±70	560	HeI
16 SE(2)	11.5	2.90	-1.49	3.26	125±40	-20±40		≥130	HeI
33 E	10	0.50	-3.38	3.42	210±60	-60±30	60±70	230	HeI
	13.5	-1.80	-2.95	3.46	80±80	110±60		140	
33 W	11	-0.50	-3.43	3.47	60±60	30±35	80±25	104	late type
21	10	2.36	-3.05	3.86	-140±50	50±40		≥150	embedded
34 W	10.5	-4.08	1.62	4.39	-80±50	-130±40	-230±70	280	HeI
3	11.5	-2.31	3.79	4.44	170±40	110±40		≥200	embedded
	13.5	-3.70	2.88	4.69	-60±100	-200±60		≥210	
7	6.5	0.20	5.55	5.55	0±60	-150±60	-130±20	200	late type
7 W	13	-3.91	5.00	6.35	70±60	-100±60	-360±80	380	HeI
	12.5	-6.30	4.60	7.80	20±60	-40±60		≥45	
	12.5	-7.10	3.75	8.03	-70±70	-120±60		≥140	
BHA 4E	11.5	-5.70	5.67	8.04	60±60	70±30	-80±30	120	late type
BHA 4W	11.5	-6.45	6.02	8.82	-270±80	170±40	100±30	330	late type
					SgrA*(IR)				
S1	15	-0.19	-0.04	0.19	650±400	-1530±400			
S2	14	0.01	0.19	0.19	-280±400	-710±400			
S3	15	0.04	-0.08	0.09	-730±600	280±600			
S4	14.5	0.15	0.04	0.12	980±400	360±450			
S5	14.5	0.21	0.04	0.21	1100±700	1240±700			
S6	14	0.36	-0.04	0.36	370±400	-140±450			
S7	15	0.51	-0.19	0.54	50±400	-30±400			
S8	14	0.19	-0.26	0.32	860±400	-310±500			
S9	15	0.11	-0.39	0.41	-330±700	-1200±700			
S10	14.5	0.06	-0.56	0.56	-940±600	-1040±600			
S11	14	0.01	-0.64	0.64	790±400	-990±400			

central point-mass plus an extended isothermal cluster of dispersion at large radii of ~ 50 km s^{-1} (providing an excellent fit to stellar mass data at projected radii p greater than a few pc: see Genzel et al. 1996 for details), we find that a central mass of 2.4×10^6 M$_\odot$ is required with high significance. The 1σ statistical uncertainty of this estimate is $\pm 0.35 \times 10^6$ M$_\odot$, with an additional systematic error resulting in a total uncertainty of ± 0.4 to $\pm 0.5 \times 10^6$ M$_\odot$. Proceeding as in Genzel et al. (1996) we have also calculated enclosed masses from the virial theorem and Bahcall-Tremaine (1981) projected mass estimators. These are defined as (Bahcall & Tremaine 1981)

$$M_{\rm v} = (3\pi/2G) \sum_i [\text{weight}\,(i)\, v_i^2] \Big/ \sum_i [\text{weight}\,(i)/p_i] \qquad (4)$$

and

$$M_{\rm BT} = \{16/\pi G \sum_i [\text{weight}\,(i)]\} \sum_i [\text{weight}\,(i) p_i v_i^2]. \qquad (5)$$

Here $p_i \sim (2/\pi) R_i$ is the projected radius of star i (radius R_i) which has weight 'weight (i)' and velocity v_i. The virial theorem implicitly assumes a homogeneous distribution of stars and equation (5) assumes that stars are in isotropic orbits dominated by a central mass. Application of these estimators to the three groups of proper motions defined above gives a mass of $2.55 \pm 0.75 \times 10^6$ M$_\odot$ within $\langle p \rangle = 0.057$ pc of the dynamic centre (24 velocities with a projected velocity dispersion of 214 ± 32 km s^{-1}), $2.65 \pm 0.6 \times 10^6$ M$_\odot$ within a projected radius of $p = 0.11$ pc (36 velocities with a pro-

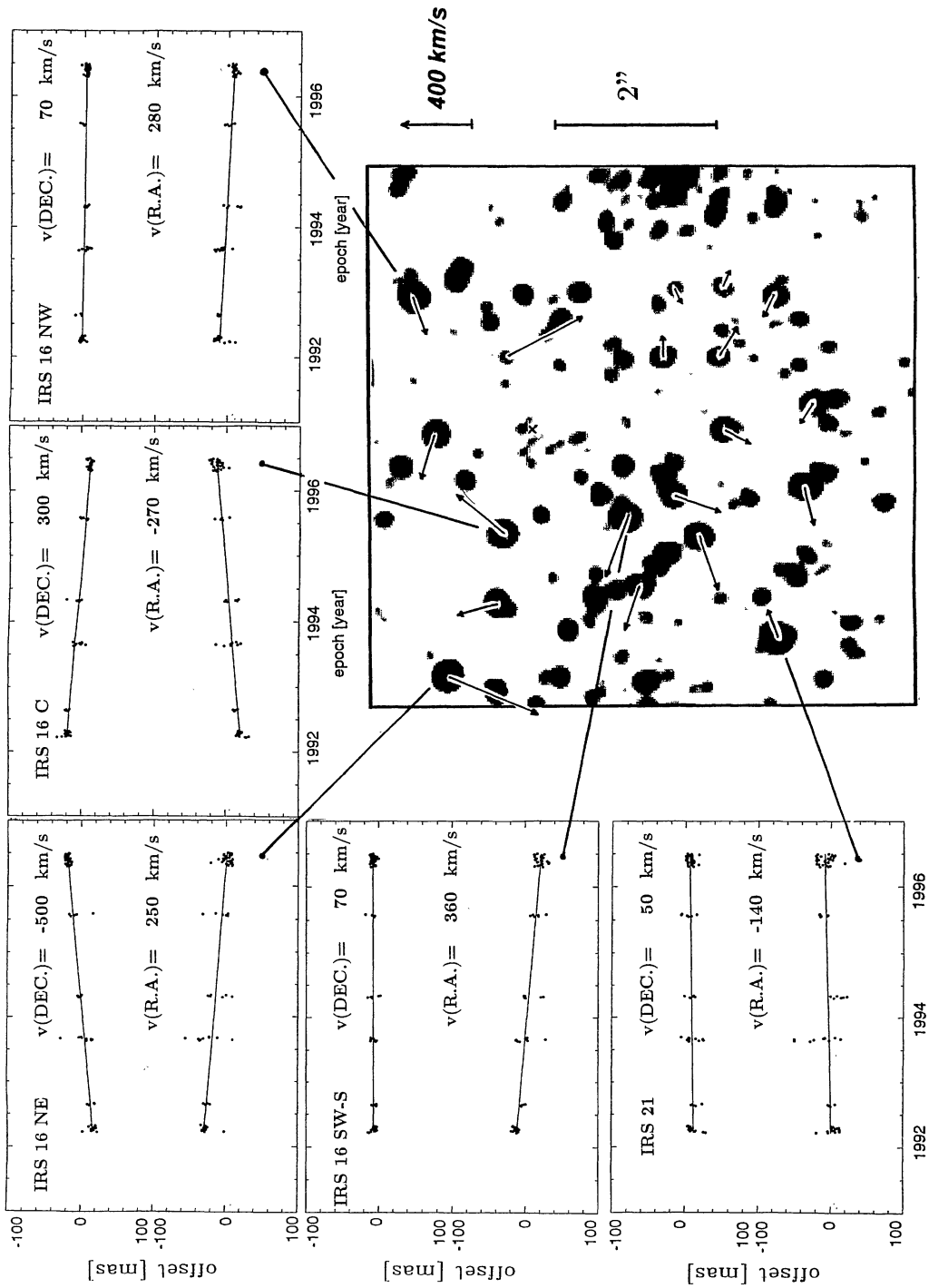

Figure 3. Proper motions and vectors in the central few arcseconds. The insets show *x*-(~RA) and *y*-(~Dec.) positions of five selected stars as a function of time, along with the best-fitting proper motions. As in Fig. 1 offsets are relative to the positions determined at the base epoch (1994.27). Positions of the different data sets in each epoch are shown as black dots, and the Dec.-graph has been offset by +200 mas. The locations of the five stars and the direction and size of their proper motion vectors (plus others from Table 2 and Fig. 1) are shown in the adjacent grey-scale 2-μm image (0.15-arcsec FWHM, Eckart et al. 1995). The cross denotes the position of Sgr A* (Eckart et al. 1995; Menten et al. 1996).

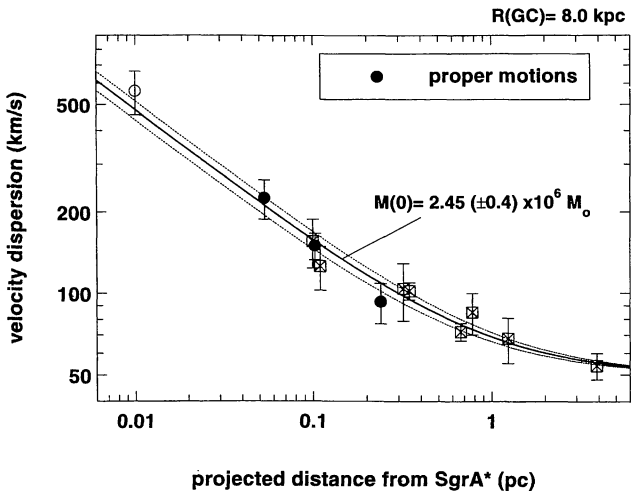

Figure 4. Projected stellar velocity dispersions as a function of projected distance from Sgr A*. Filled circles (and 1σ statistical error bars) represent the dispersions (corrected for measurement bias, see Genzel et al. 1996) derived from the present proper motion data for 39 stars between 0.035 and 0.34 pc (RA and Dec. motions combined and separated into three independent groups of between nine and 18 stars each). The open circle denotes our preliminary estimate of the proper motion velocity dispersion obtained from the 11 components (22 motions) of the Sgr A* (IR) cluster, corrected for measurement bias. Open rectangles represent radial velocity dispersion data, taken from Rieke & Rieke (1988), McGinn et al. (1989), Sellgren et al. (1990), Lindqvist et al. (1992), Haller et al. (1996) and Genzel et al. (1996). The solid curve is the best fit of the stellar dynamics with an isotropic velocity field in the potential of a point mass ($2.45 \times 10^6\,M_\odot$) plus an isothermal cluster with one-dimensional dispersion at infinity of 50 km s^{-1}. This dispersion (which is added in squares to the dispersion caused by the central dark mass) accounts for the background mass of the (visible) stellar cluster (Genzel et al. 1996). The dotted curves represent the $\pm 1\sigma$ total uncertainties ($\pm 0.4 \times 10^6\,M_\odot$), consisting of the fit uncertainties ($\pm 0.24 \times 10^6\,M_\odot$) and systematic errors.

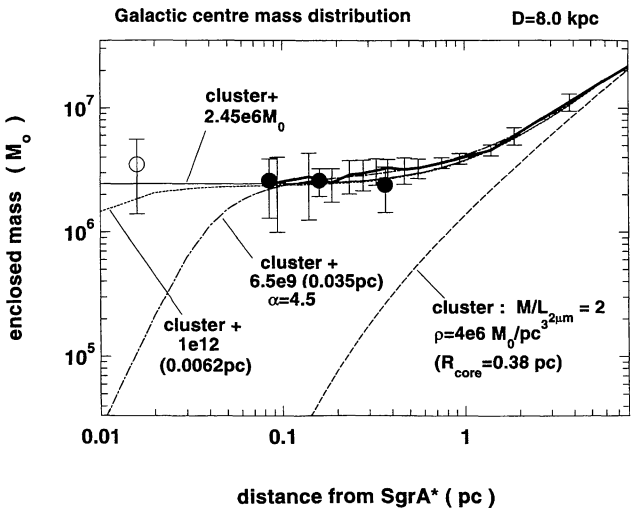

Figure 5. Mass modelling of the stellar proper and radial motions (for a Sun–Galactic Centre distance of 8.0 kpc). The thick curve (with 1σ error bars) gives the enclosed mass as a function of distance from Sgr A* derived from the Jeans equation mass modelling of the stellar radial velocities, assuming anisotropy $\delta = 0$ (Genzel et al. 1996 and references therein). Filled circles and 1σ error bars denote the masses estimated from independent Jeans' modelling of the proper motions for 39 stars (78 motions) between 0.9 and 8.8 arcsec, again for $\delta = 0$. The open circle (and combined statistical and systematic error bar) denotes our preliminary mass estimate from the motions in the Sgr A* (IR) cluster. The thick dashed curve represents the mass model of the stellar cluster observed in the near-infrared [$M/L(2\ \mu m) = 2$, $R_{core} = 0.38$ pc, $\rho(R=0) = 4 \times 10^6\,M_\odot\,pc^{-3}$]. The thin continuous curve is the sum of the visible stellar cluster plus a central $2.45 \times 10^6\,M_\odot$ point mass. The thin dash–dotted curve is the sum of the visible cluster plus a dark cluster of core radius 0.035 pc and central density $6.5 \times 10^9\,M_\odot\,pc^{-3}$. For $R \gg 0.035$ pc the dark cluster density is proportional to $R^{-4.5}$. The dotted curve is the sum of the visible cluster and a dark cluster of core radius 0.0062 pc and central density $10^{12}\,M_\odot\,pc^{-3}$.

jected velocity dispersion of 152 ± 18 km s^{-1}) and $2.12 \pm 0.7 \times 10^6\,M_\odot$ within a projected radius of $p = 0.24$ pc (18 velocities with a projected velocity dispersion of 93 ± 16 km s^{-1}). Virial and Bahcall–Tremaine estimators give essentially the same values.

A better way of deriving the mass distribution $M(R)$ enclosed within R without having to assume a dominating central mass and an isotropic velocity field – as required when using the Bahcall–Tremaine and virial theorem estimators – is the first-order moment of the collisionless Boltzmann equation (the 'Jeans' equation). This equation can be applied for an ensemble of stars with spherically symmetric space density distribution $n(R)$ in a gravitational potential $\Phi(R)$ (Binney & Tremaine 1987, chapter 4):

$$\Phi(R) = GM(R)/R = v_{rot}(R)^2 + \sigma_r(R)^2 \qquad (6)$$
$$\times \{ -\mathrm{d}\ln[n(R)]/\mathrm{d}\ln R - \mathrm{d}\ln[\sigma_r(R)^2]/\mathrm{d}\ln R - 2\delta \}.$$

This equation includes the anisotropy parameter $\delta = 1 - \sigma_\theta(R)^2/\sigma_r(R)^2$ for the azimuthal and radial velocity distributions. For an isotropic velocity dispersion $\delta = 0$. To apply the Jeans equation to the data it is necessary to transform from intrinsic dispersions $\sigma(R)$ and volume densities $n(R)$ to projected dispersions $\sigma(p)$ and surface densities $\Sigma(p)$ via Abel integral equations, or vice versa. We decided to start with parametrized models for the intrinsic quantities and then fit the observed quantities after numerically integrating the Abel integral equations. This method is preferable to the reverse procedure, which is very sensitive to individual data points and their errors (Kormendy & Richstone 1995). A detailed description of this procedure is given in Genzel et al. (1996, see also Saha, Bicknell & McGregor 1996). In the following, the way in which we treat the issue of anisotropy is to regard the radial and proper motion data as two independent data sets, apply equation (6) with $\delta = 0$ to either one, and see how well the results agree. In Fig. 5 the Jeans equation mass model derived from the radial velocity data is the thick continuous curve (plus 1σ error bars, taken from fig. 12b of Genzel et al. 1996). The filled circles (with 1σ error bars) mark the Jeans equation mass model for the new proper motion data (again for $\delta = 0$), using the source number counts for $m(K) \leq 13.5$ of Eckart et al. (1995) as the basis for deriving $n(R)$ and the three projected velocity dispersions given above to derive $\sigma(R)$. Again, radial and proper motion Jeans mass models are in excellent agreement, implying that the anisotropy is very close to zero. Assuming now $\delta = 0$, the combined radial

and proper motion data at projected radii of $p \geq 0.057$ pc is clearly very well fitted by a combination of a dark point-mass plus the extended cluster of stars radiating in the near-infrared. The thin curve in Fig. 5 is a combination of a $2.45 \times 10^6\,M_\odot$ point-mass plus the visible (isothermal) stellar cluster of core radius 0.38 pc and core stellar density of $4 \times 10^6\,M_\odot\,pc^{-3}$, representing the stellar cluster radiating in the near-infrared with an M/L (2 μm) ratio of about 2 (Genzel et al. 1996). The statistical significance for the dark central mass is somewhere between 10 and 6σ, depending on whether just the statistical, or the combined statistical and systematic, error bars are considered.

The dash–dotted curve in Fig. 5 is the combination of the same visible stellar cluster with a second, dark cluster of non-zero core radius. To fit the data, the central dark cluster must have a central density of at least $6.5 \times 10^9\,M_\odot\,pc^{-3}$ and a core radius of less than 0.035 pc. Note that to fit the flat observed mass distribution in the range between 0.1 and 1 pc its density must scale as $R^{-4.5}$.

Where is the dark mass concentration centred? While eventually a detailed analysis based on orbit fitting for all stars with three space velocities should give the most accurate result, a simple analysis can already be obtained now from the directions for ~15 best proper motion vectors within ~3 arcsec of Sgr A*. Assuming that all stars are on circular orbits about the dynamic centre, the location of that centre should lie on a line perpendicular to the direction of proper motion. For the stars within ~3 arcsec of Sgr A* there is a reasonably well-defined crossing point of these lines located 0.015 ± 0.02 pc east of Sgr A* (Menten et al. 1996).

3.3 The Sgr A* (IR) cluster

The proper motion data thus strongly suggest that the dark mass concentration is located very close to or on the compact radio source Sgr A*. Its location relative to the near-infrared stellar distribution [a cross in Fig. 2 and (0, 0) in Fig. 6] has recently been determined by Menten et al. (1996) to be ±30 mas. Sgr A* lies approximately at the centre of a 'hammer'-shaped concentration of fainter stars [Sgr A* (IR): Eckart et al. 1995]. Eckart et al. (1995) have concluded that the Sgr A* (IR) cluster may in fact be a local concentration of either late-type giants of late-O/early-B stars in the immediate vicinity of Sgr A*, on a scale of 0.01 pc. Therefore, if the central dark mass is physically associ-

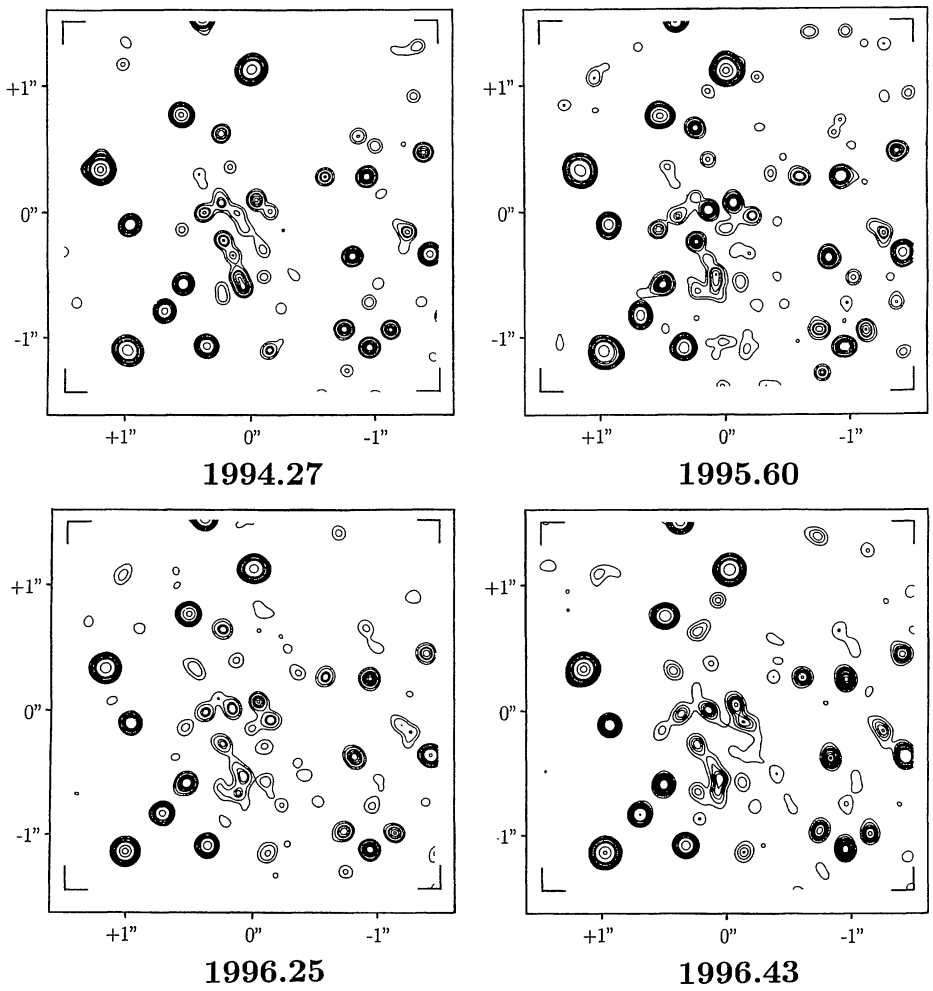

Figure 6. 2.2-μm Lucy-CLEANed maps (FWHM 0.15 arcsec) of the central Sgr A* (IR) cluster, taken in 1994, 1995 and 1996, and referred to the radio position of Sgr A* at (0, 0) (Menten et al. 1996). The bright star in the north is IRS 16 NW.

ated with Sgr A* these faint stars may be the ultimate test particles for pinpointing the centroid and better determining the density of the dark mass. Fig. 6 shows a series of the four best images of Sgr A* (IR) we were able to obtain between 1994 and 1996. Unfortunately, the data quality prior to 1994 was not as good, partly as a result of a poorer sensitivity of the camera and partly because of worse seeing. The data set in 1995 is also not as good as the 1994 and the two 1996 data sets. However, in all four images the Sgr A* (IR) cluster is reasonably well resolved into about 12 components. A visual inspection of the four images shows that the two images in 1996 are very similar while there are fairly obvious structural changes between 1994 and 1996. These are especially striking in the region of the S1, S2 and S3 components and in the region of the S8–S11 components (see Fig. 10 for the nomenclature of these components). The morphology of the 1995 epoch map ranges somewhere between those of the 1994 and 1996 data. This suggests that there are secular changes of the source structure which again may be indicative of stellar proper motions.

The Sgr A* (IR) complex is faint and crowded (the individual components have K magnitudes between 14 and 15) and it is therefore crucial to ascertain that the structural changes are intrinsic to the source, and not caused by the fairly complex data reduction. For this purpose we display in Fig. 7 two independent maps for each of the four epochs. Fig. 8 shows raw SSA maps, as well as high-pass-filtered SSA maps ('smooth-subtracted' SSA maps). Finally, we show for comparison in Fig. 9 raw and smooth-subtracted SSA maps of a region with similar brightness stars ~1.5 arcsec west of Sgr A*. Note that none of the raw maps in Figs 7 to 9 are astrometric, so that a very slight stretch/compression and, in particular, an overall rotation is allowed for best comparison between different data sets. From Figs 6 to 9 we conclude the following.

(i) The derived Sgr A* (IR) source structure is quite reliable. It is definitely not seriously affected by the data reduction techniques. Maps within a given epoch and the two 1996 epoch maps are very similar. The basic components/structure of the source is fully recognizable even in the raw SSA maps (although less so for the 1995 data sets). Smooth-subtracted SSA maps and Lucy-CLEANed maps compare well. The sources S1–S11 are detected with quite good signal-to-noise ratio (10 to 50:1). The faintness of the Sgr A* (IR) region is to some degree compensated for by the fact that it was observed in all data sets, near the centre of the frames.

(ii) There are fairly obvious source structure changes that consistently continue from the earliest through to the last

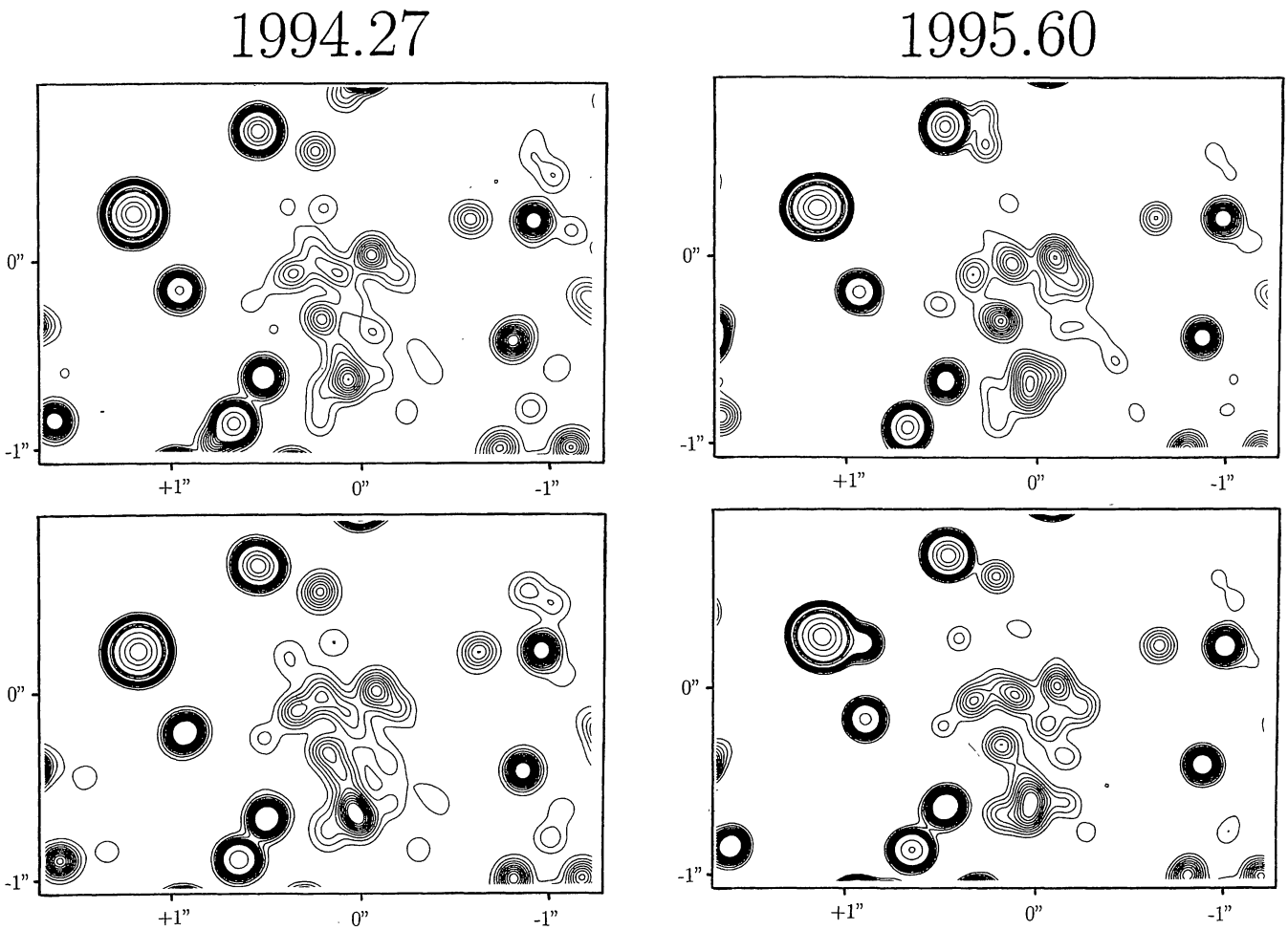

Figure 7. Comparison of two independent Lucy-CLEANed maps of Sgr A* (IR), for each of the four epochs. The angular resolution is 0.18 arcsec FWHM. The combination of higher resolution maps in each epoch results in the images displayed in Fig. 6.

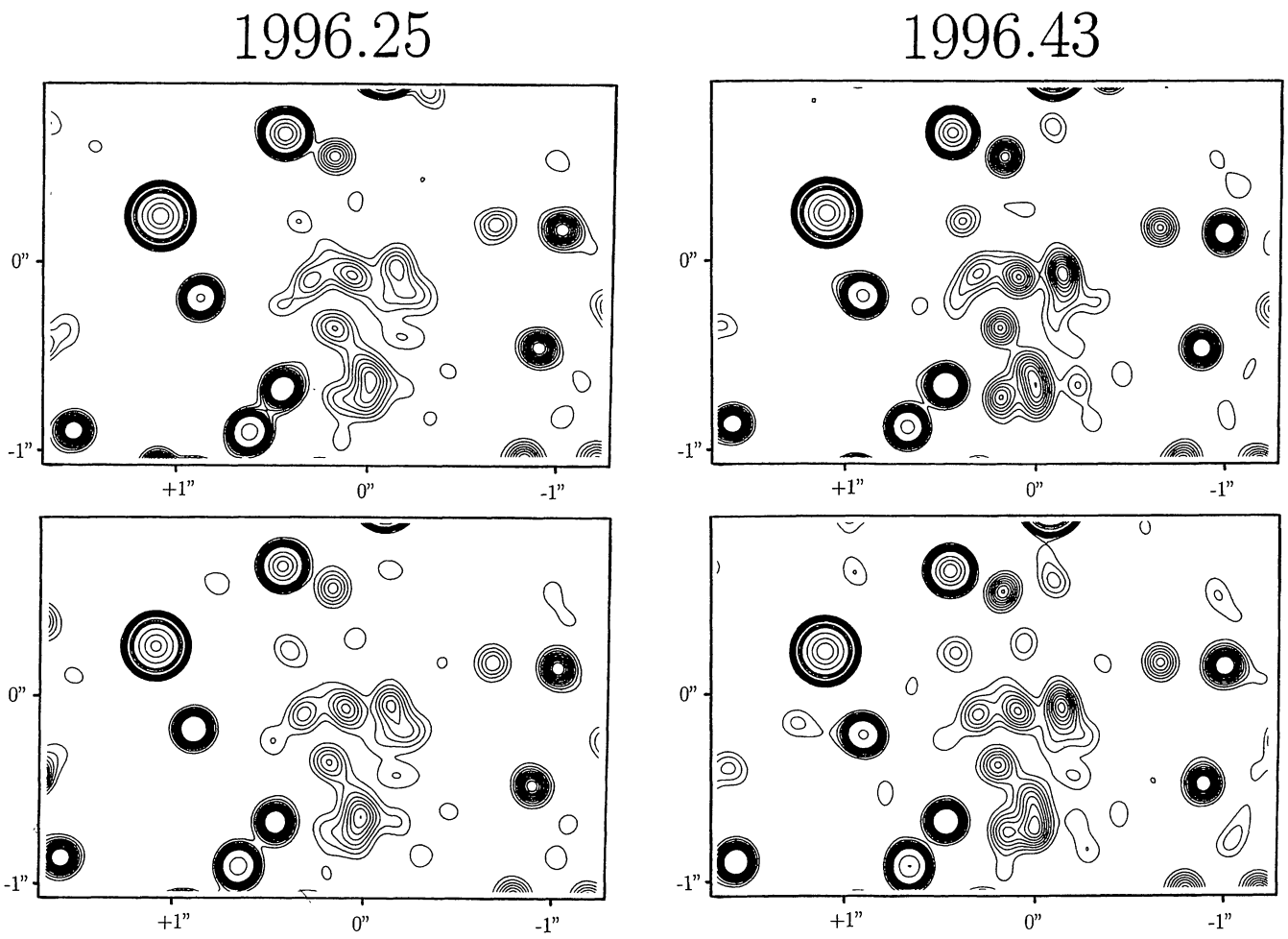

Figure 7 – *continued*

period. As mentioned above, the most obvious changes are in the triangle S1–S2–S3 and in the chain S8–S11. In addition, there appear to be changes that probably have to be ascribed to variability. For instance, S3, S5 and S9 seem to be becoming weaker with time.

(iii) In the comparison field 1.5 arcsec west of Sgr A* (IR) no such secular changes are seen. Using the same data sets and reduction techniques as for Sgr A* (IR), proper motions in that field are less than about 500 km s^{-1}.

We thus conclude that *we have probably detected orbital proper motions in the Sgr A* (IR) cluster as well* (see Section 3.4 for a brief discussion of gravitational lensing). Fig. 10 is a first attempt at constructing position–time diagrams and proper motion vector maps for the components of the Sgr A* (IR) cluster. The inferred proper motions are added in the last 11 rows of Table 2. Several of the stars in Sgr A* (IR) appear to move with total proper motions of 1000 to 1600 km s^{-1}. Probably the most convincing case is S1 (relative to S2/S3), which is within 0.2 arcsec (0.008 pc) of Sgr A*. S1 appears to move with 1600 ± 400 km s^{-1} with respect to the overall base position and with 1950 ± 500 km s^{-1} relative to the centroid of S1/S2. While the individual motions are still poorly determined ($< 4\sigma$, Table 2), one still has to worry about the influence of variability and the data clearly need to be improved: the derived velocity dispersion (560 ± 90 km s^{-1} at $p = 0.01$ pc, corrected for measurement bias) already appears statistically significant. Of course there is a significant systemic error, in addition to the statistical error of ± 90 km s^{-1}. This systematic error has to do with the source decomposition, data reduction and variability, so that the overall error is probably twice as large as the statistical error. We therefore regard the evidence for a very large velocity dispersion in Sgr A* (IR) at this point still as preliminary. Nevertheless the value derived above in fact fits very well on the extrapolations of the models shown in Figs 4 and 5. Inclusion of this innermost point in the fitting gives a best-fitting value for the central mass of $2.45\{\pm 0.25$ statistical$\}$, $\{\pm 0.4$ total$\}$ $\times 10^6 M_\odot$. If confirmed, this large velocity dispersion shows that the dark mass is concentrated and centred within ≤ 0.009 pc of Sgr A*. Mass modelling with a dark cluster shows that its density then would have to be $\geq 10^{12} M_\odot$ pc^{-3} and its core radius ≤ 0.0062 pc (dotted in Fig. 5).

3.3 Effects of gravitational lensing

Can the structural changes of the Sgr A* (IR) cluster be caused by gravitational lensing? Let us assume that there is a central massive object of $M_{2.5} = M/2.5 \times 10^6 M_\odot$, surrounded by a dense cluster of stars. The surface density of the Sgr A* (IR) cluster (~ 8.5 source arcsec^{-2}) is 2.8 ± 1

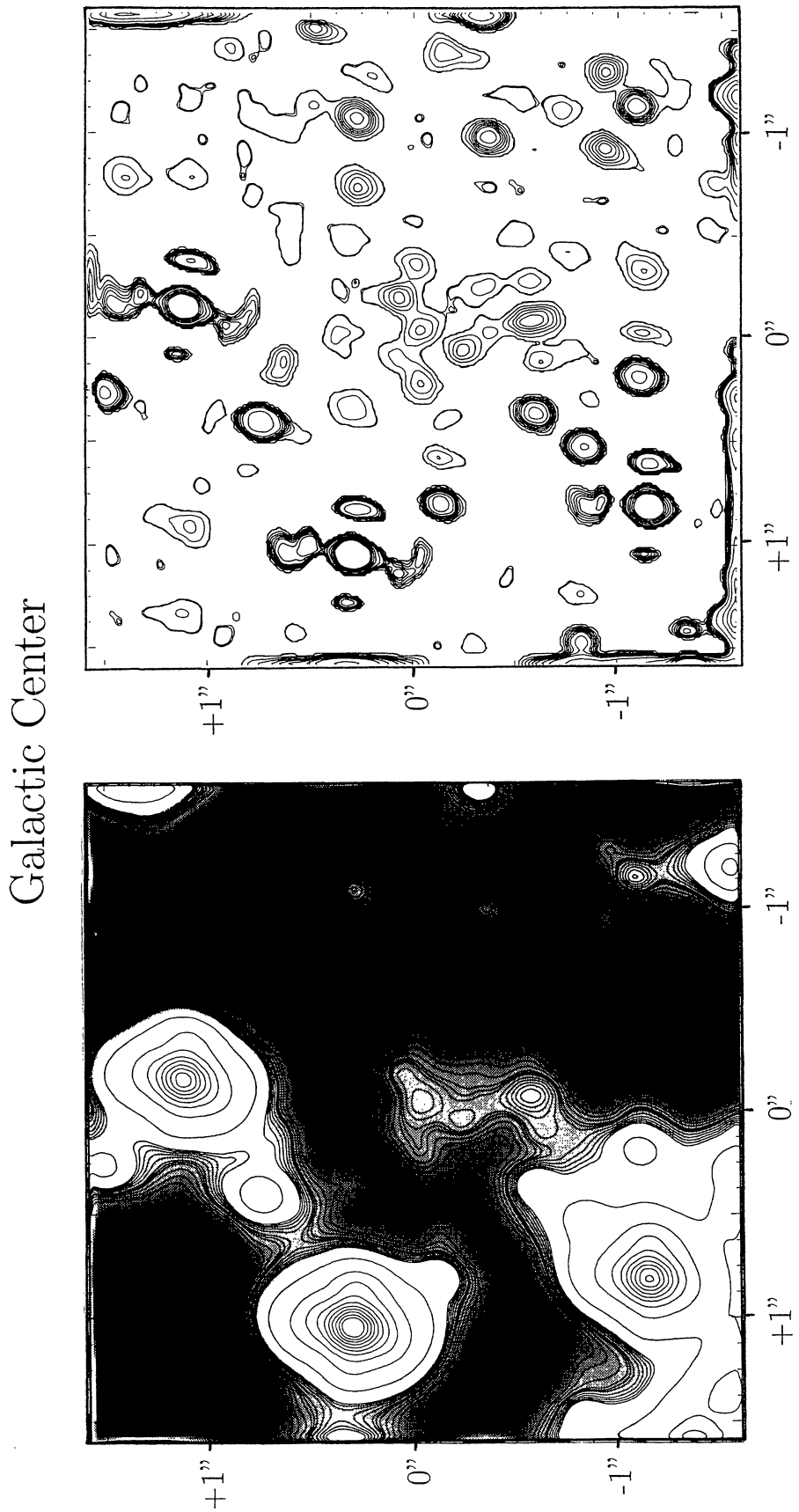

Figure 8. Raw SSA and high-pass-filtered (smooth-subtracted) SSA maps of the Sgr A* (IR) cluster. On the grey-scale versions of the raw SSA maps (left) a contour version of the same map has been overlaid. The smooth-subtracted versions of the maps (right) have been produced by convolving the raw SSA maps with a 0.1-arcsec FWHM Gaussian, subtracting it from the raw map and (for display purposes) convolving the difference with the same Gaussian. The resulting maps are smoothed versions of the diffraction-limited parts of the raw SSA images that contain all the remaining telescope artefacts. Despite a different representation the structure of the Sgr A* (IR) cluster is very similar to the cleaned version in Fig. 6.

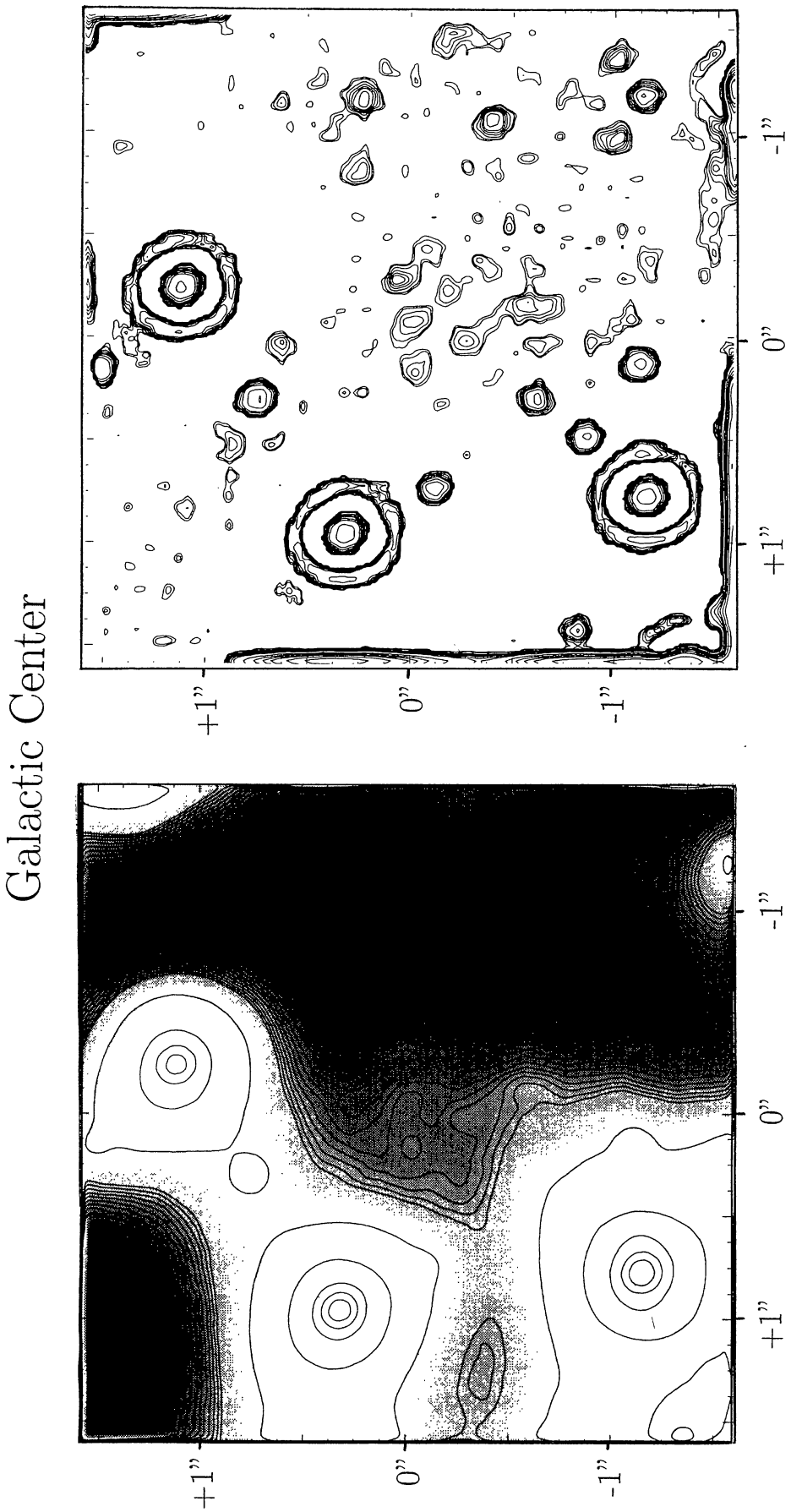

Figure 8 – *continued*

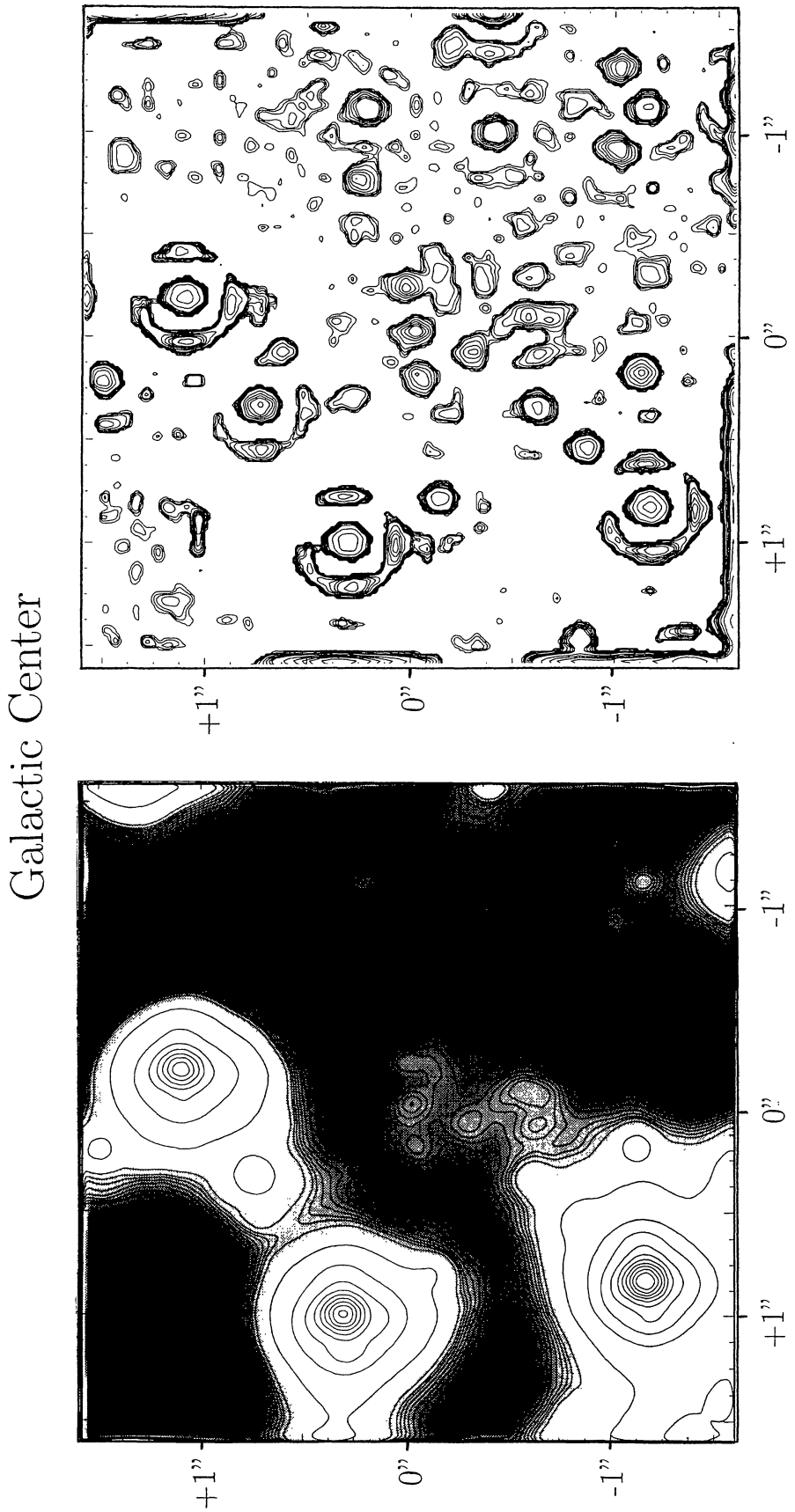

Figure 8 – *continued*

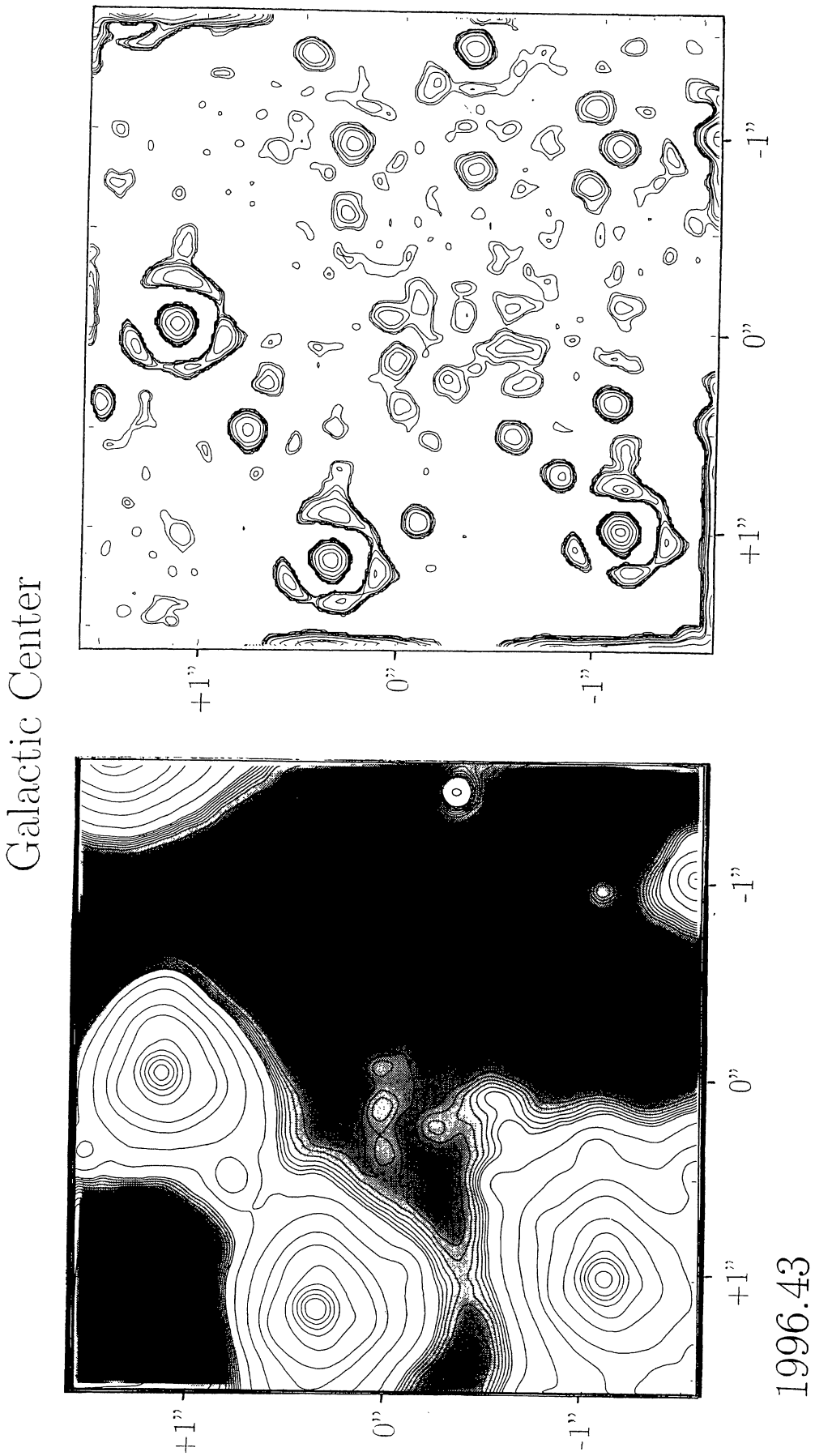

Figure 8 – *continued*

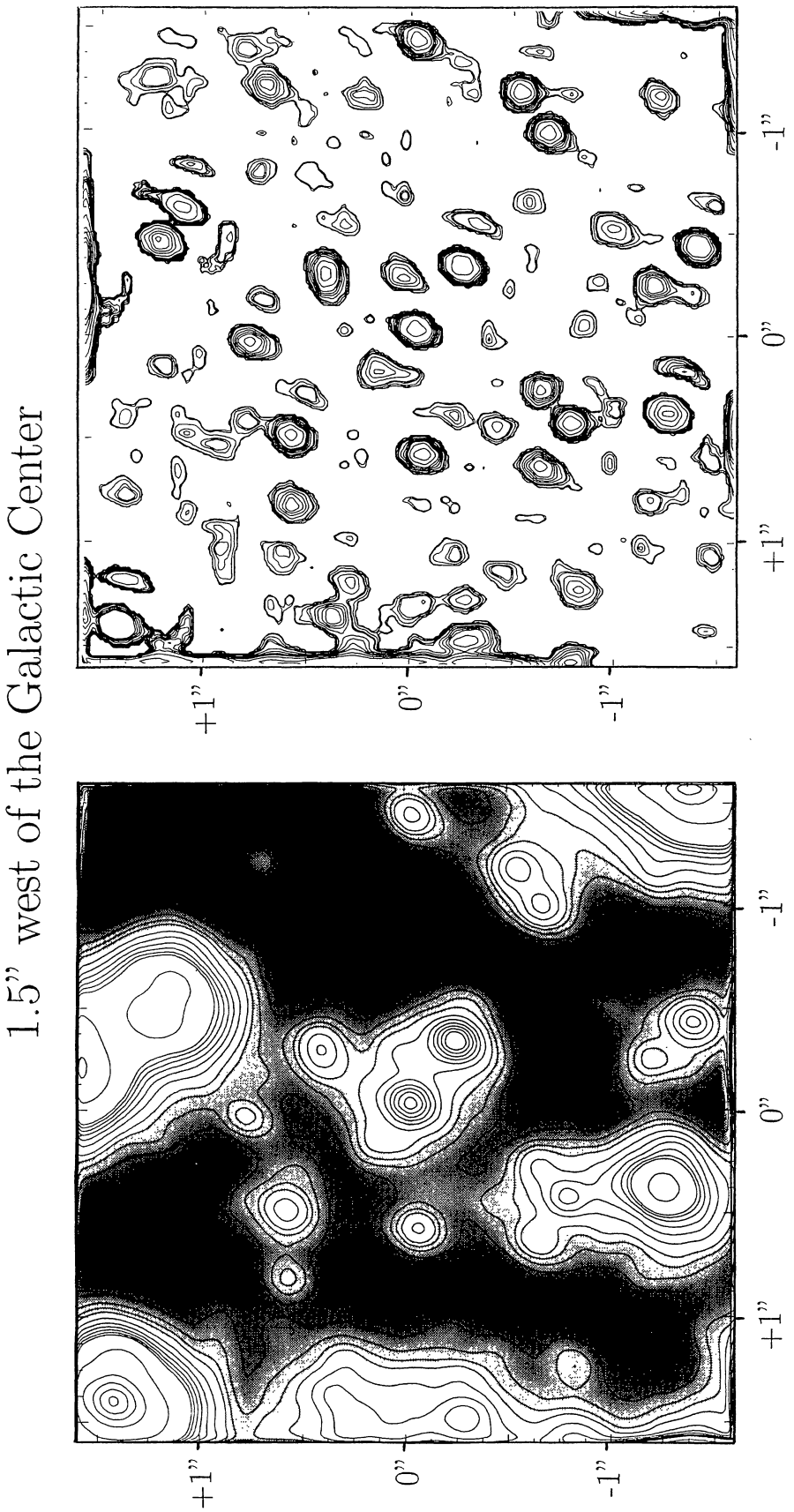

Figure 9. Raw SSA and smooth-subtracted SSA maps of a region 1.5 arcsec west of the Sgr A* (IR) region (visible at the left edge), containing groupings of stars of similar fluxes (see caption for Fig. 8).

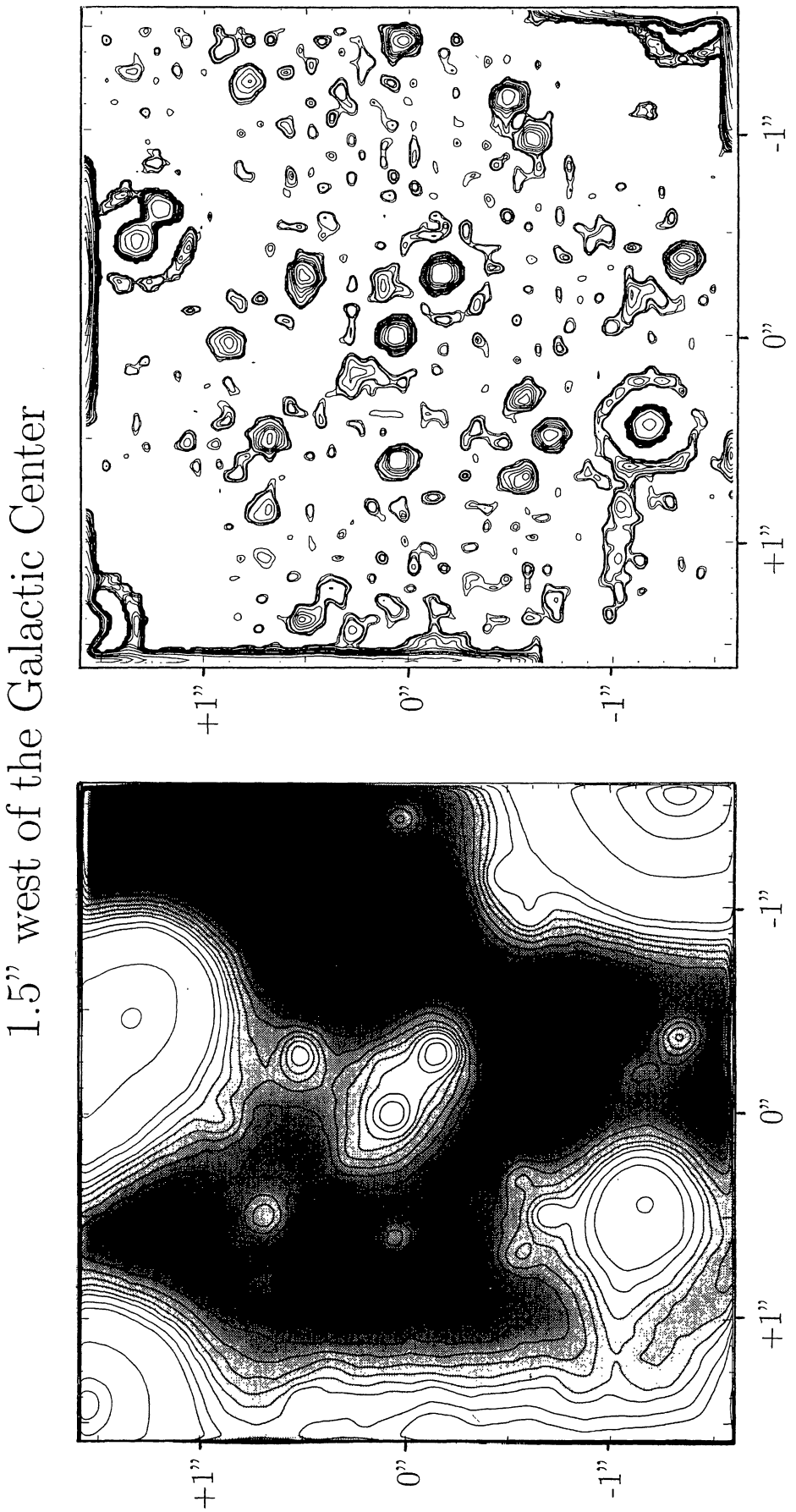

Figure 9 – *continued*

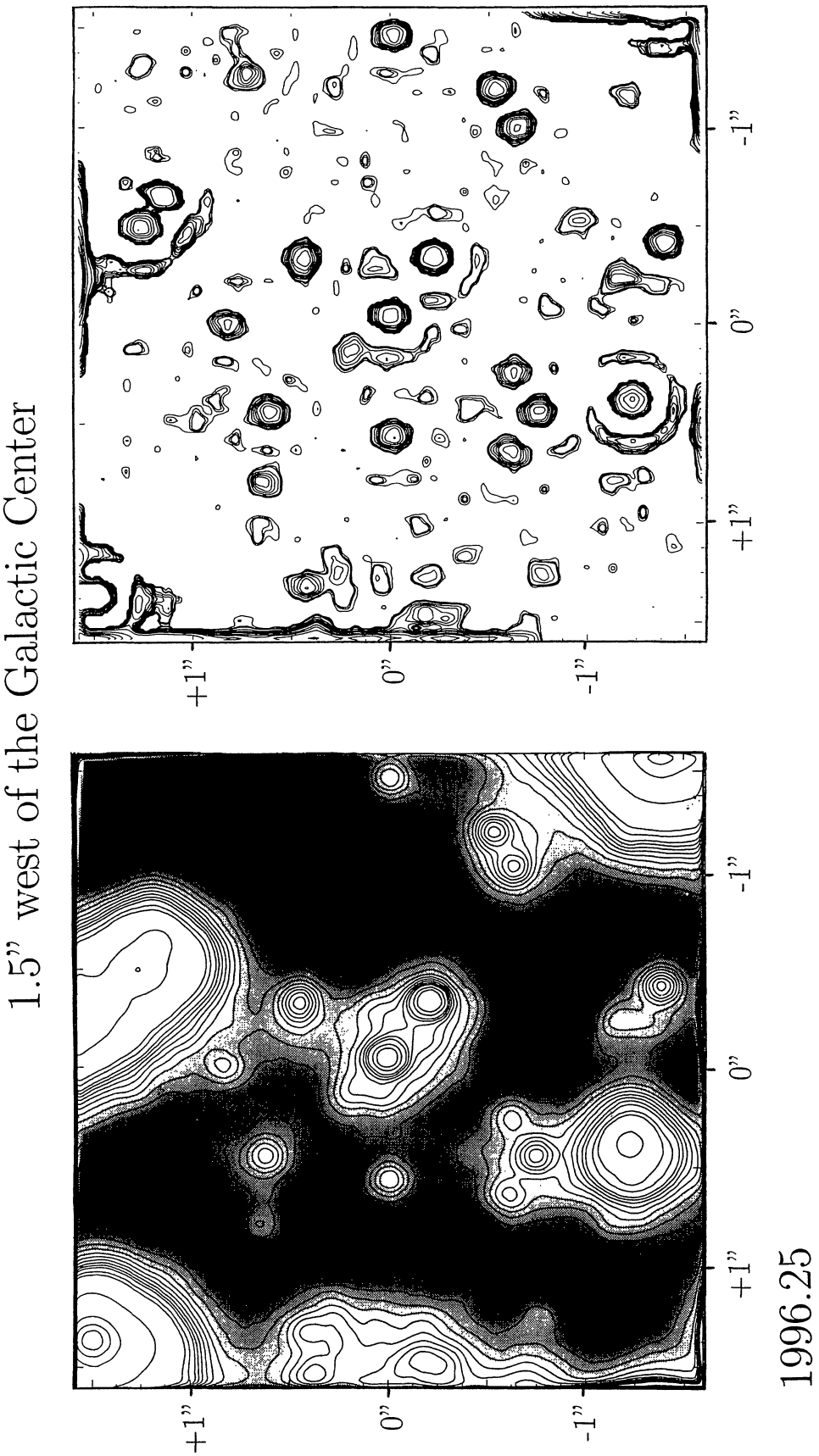

Figure 9 – *continued*

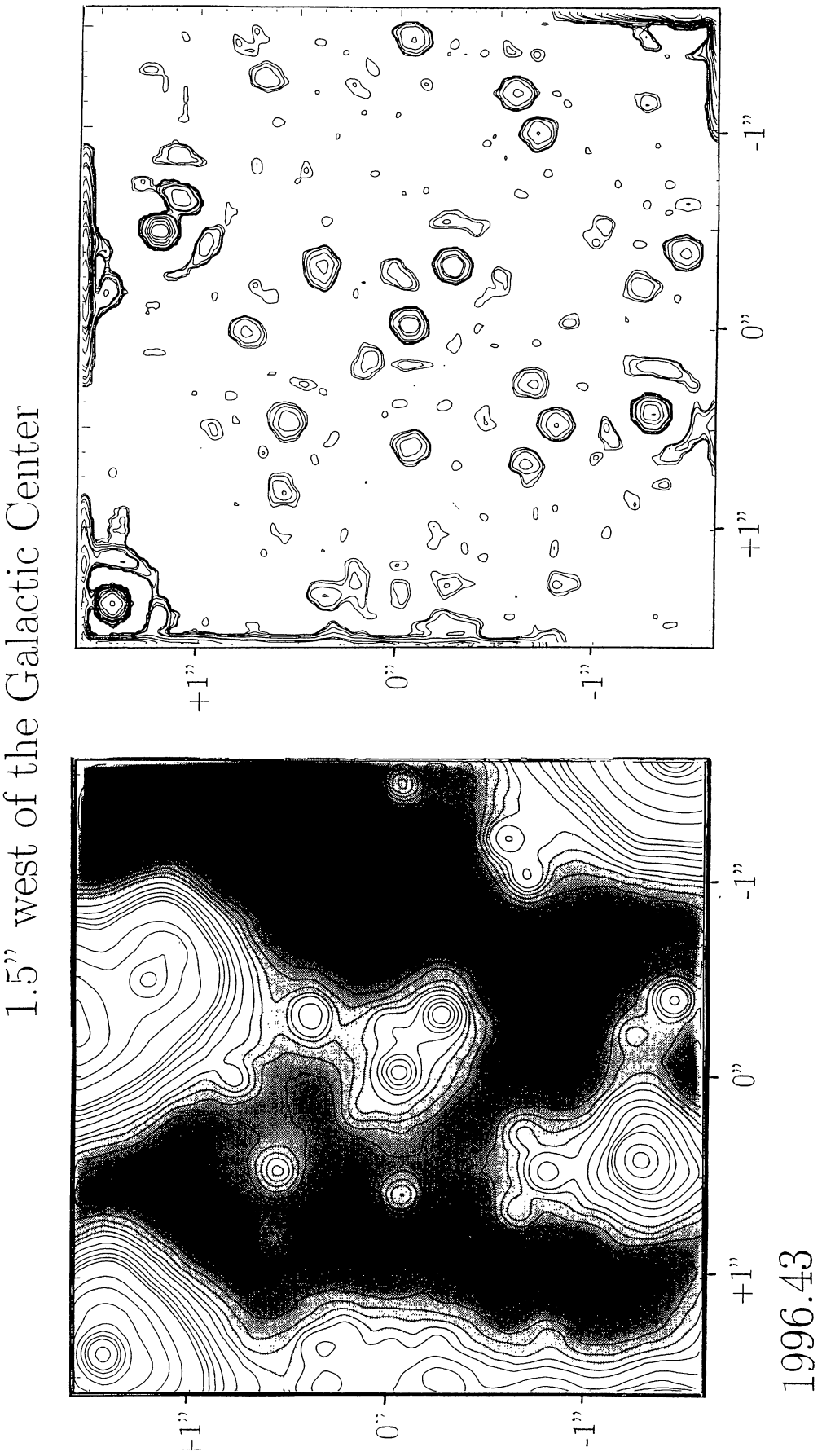

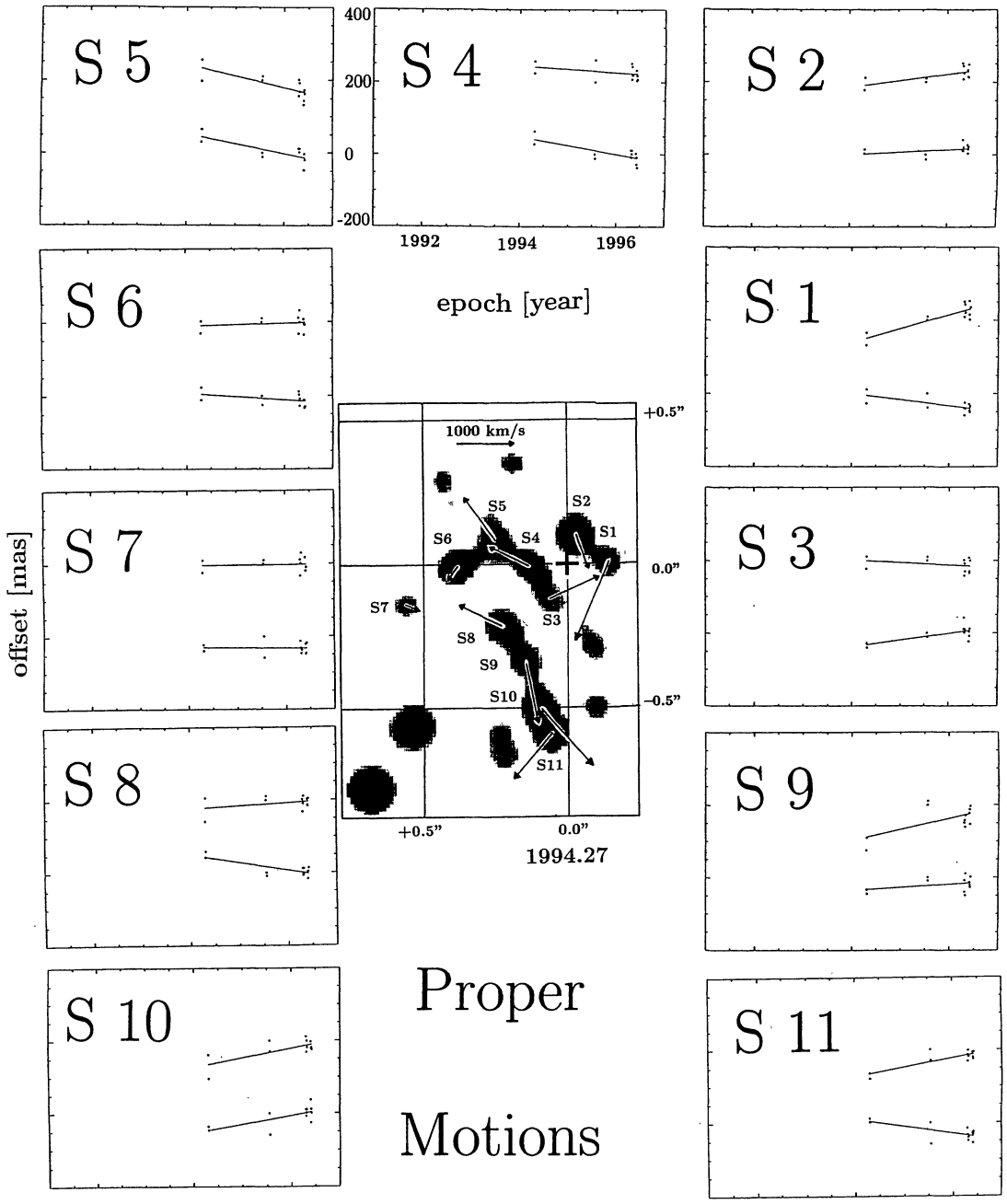

Figure 10. Derived positions as a function of time (epochs 1994.27, 1995.6, 1996.25, 1996.43) for the S1–S11 components of Sgr A* (IR), along with best-fitting proper motions shown as straight lines (Table 2). The central panel shows the proper motion vectors on a schematic map of the Sgr A* (IR) region.

times larger than the peak density elsewhere within the core radius ($\sim$0.1 to 0.2 pc) of the stellar distribution down to $K\sim 15$ (Eckart et al. 1995). This strongly suggests that the Sgr A* (IR) stars have to be within $R \leq 0.2$ pc of the compact radio source. The Einstein ring angle of a star at radius R from the central mass then is (e.g. Wardle & Yusef-Zadeh 1992)

$$\theta_E = 2\{GMR/[(R+R_\odot)R]\}^{0.5}/c = 8M_{2.5}^{0.5}R_{0.2}^{0.5} \quad \text{(mas)}. \quad (7)$$

$R_\odot = 8$ kpc is the Sun–Galactic Centre distance. Substantial magnification occurs only within true angular separations from the central mass of $\chi \leq \theta_E$. The size of the Sgr A* (IR) cluster is about 70 times larger than that and the changes in positions of the faintest moving stars (1 to 1.6×10^3 km s^{-1})

over the last years correspond to 50 to 90 mas. Moreover the time-scale for significant lensing Δt_l is approximately given by

$$\Delta t_l \leq \theta_E R_\odot / v_p. \quad (8)$$

Since the proper motion velocities in the core v_p are typically of a few hundred km s^{-1}, these gravitational lens effects will last about a year for low magnification and much less for high magnification. The Sgr A* (IR) cluster has, however, had about the same appearance for the last two and probably for the last four years.

We thus conclude that it is highly unlikely that the structural changes we have seen in the Sgr A* (IR) cluster are caused by gravitational lensing. This conclusion is consistent with the considerations of Wardle & Yusef-Zadeh (1992) who also find that gravitational lens effects cannot be detected using the present methods.

4 CONCLUSIONS

The Galactic Centre and the 'megamaser' galaxy NGC 4258 (Greenhill et al. 1995; Myoshi et al. 1995) are now known to contain dark central mass concentration with densities significantly exceeding $10^9\,M_\odot\,pc^{-3}$. What is the nature of this dark mass? Given that the dark mass in the Galactic Centre is now constrained to be at least 10 times more concentrated and therefore 1000 times denser than the visible stellar cluster, we can now exclude with some confidence the possibility that it consists of a cluster of solar mass remnants (neutron stars or white dwarfs: see the detailed discussion in Genzel et al. 1996). Considering the stellar dynamics outside $R \sim 0.05$ pc, the remaining possibilities are a core-collapsed cluster of 10–20 $M_\odot$ stellar black holes (Morris 1993; Lee 1995), or a single massive black hole, or a combination thereof. If the Sgr A* (IR) cluster evidence were to be confirmed the only remaining viable configuration is a single, compact, massive object. The main reason is that in the models of Lee (1995) the half-mass radius even for a core-collapsed cluster of 10–20 $M_\odot$ stellar black holes is much greater than the core radius implied by the innermost point in Fig. 5. Current theory tells us that this compact massive object must be a massive black hole.

ACKNOWLEDGMENTS

A number of people at MPE and ESO have been involved in making this experiment possible and carrying it out. We especially thank N. Ageorges, S. Drapatz, R. Hofmann, A. Krabbe, B. Sams, L. E. Tacconi-Garman and H. van der Laan. We are grateful to C. H. Townes for very helpful advice.

REFERENCES

Bahcall J. N., Tremaine S., 1981, ApJ, 244, 805
Binney J. J., Tremaine S. C., 1987, Galactic Dynamics. Princeton Univ. Press, Princeton
Christou J. C., 1991, Exp. Astron., 2, 27
Eckart A., Genzel R., 1996, Nat, 382, 47
Eckart A., Genzel R., Krabbe A., Hofmann R., van der Werf P. P., Drapatz S., 1992, Nat, 355, 526
Eckart A., Genzel R., Hofmann R., Sams B. J., Tacconi-Garman L. E., 1993, ApJ, 407, L77
Eckart A., Genzel R., Hofmann R., Sams B. J., Tacconi-Garman L. E., Cruzalebes P., 1994, in Genzel R., Harris A. I., eds, The Nuclei of Normal Galaxies. Kluwer, Dordrecht, p. 305
Eckart A., Genzel R., Hofmann R., Sams B. J., Tacconi-Garman L. E., 1995, ApJ, 445, L26
Genzel R., Watson D. M., Crawford M. K., Townes C. H., 1985, ApJ, 297, 766
Genzel R., Thatte N., Krabbe A., Kroker H., Tacconi-Garman L. E., 1996, ApJ, 472, 153
Greenhill L. J., Jiang D. R., Moran J. M., Reid M. J., Lo K. Y., Claussen M. J., 1995, ApJ, 440, 619
Haller J. W., Rieke M. J., Rieke G. H., Tamblyn P., Close L., Melia F., 1996, ApJ, 456, 194
Hofmann R., Blietz M., Duhoux P., Eckart A., Krabbe A., Rotaciuc V., 1993, in Ulrich M. H., ed., Progress in Telescope and Instrumentation Technologies. ESO Report 42, p. 617
Knox K. T., 1976, J. Opt. Soc. Am., 66, 1236
Kormendy J., Richstone D., 1995, ARA&A, 33, 581
Krabbe A. et al., 1995, ApJ, 447, L95
Lacy J. H., Townes C. H., Geballe T. R., Hollenbach D. J., 1980, ApJ, 241, 132
Lacy J. H., Achterman J. M., Serabyn E., 1991, ApJ, 380, L71
Lee H. M., 1995, MNRAS, 272, 605
Lindqvist M., Habing H., Winnberg A., 1992, A&A, 259, 118
Lohmann A. W., Weigelt G., Wirnitzer B., 1983, Appl. Opt., 22 (24), 4028
Lucy L. B., 1974, AJ, 79, 745
McGinn M. T., Sellgren K., Becklin E. E., Hall D. N. B., 1989, ApJ, 338, 824
Menten K. M., Eckart A., Reid M. J., Genzel R., 1996, ApJ, in press
Morris M., 1993, ApJ, 408, 496
Myoshi M., Moran J. M., Hernstein J., Greenhill L., Nakai N., Diamond P., Inoue M., 1995, Nat, 373, 127
Reid M., 1993, ARA&A, 31, 345
Rieke G. H., Rieke M. J., 1988, ApJ, 330, L33
Rosa M. R., Zinnecker H., Moneti A., Melnick J., 1992, A&A, 257, 515
Saha P., Bicknell G. Y. V., McGregor P. J., 1986, PASP, in press
Sellgren K., McGinn M. T., Becklin E. E., Hall D. N. B., 1990, ApJ, 359, 112
Serabyn E., Lacy J H., 1985, ApJ, 293, 445
Simon M., Chen W. P., Forrest W. J., Garnett J. D., Longmore A. J., Gauer T., Dixon R. I., 1990, ApJ, 360, 95
Simons D. A., Hodapp K. W., Becklin E. E., 1990, ApJ, 360, 106
Wardle M., Yusef-Zadeh F., 1992, ApJ, 387, L65
Wollman E., 1976, PhD thesis, Univ. of California, Berkeley